









RESEARCH ARTICLE

10.1029/2024MS004522

Special Collection:

The CliMA Earth System Model

Formulation and Calibration of CATKE, a One-Equation Parameterization for Microscale Ocean Mixing

Gregory LeClaire Wagner¹ , Adeline Hillier¹ , Navid C. Constantinou^{2,3} , Simone Silvestri¹, Andre Souza¹ , Keaton J. Burns¹, Chris Hill¹ , Jean-Michel Campin¹, John Marshall¹ , and Raffaele Ferrari¹

¹Massachusetts Institute of Technology, Cambridge, MA, USA, ²University of Melbourne, Parkville, VIC, Australia, ³ARC Center of Excellence for the Weather of the 21st Century, Parkville, VIC, Australia

Key Points:

- We describe a new parameterization called CATKE with a convective adjustment (CA) component and prognostic turbulent kinetic energy (TKE)
- We make extensive use of Ensemble Kalman Inversion calibration to 21 idealized large eddy simulations (LES) to guide CATKE's development
- We validate CATKE by interpreting its free parameters and comparing to additional idealized and realistic LES

Correspondence to:

G. L. Wagner,
wagner.greg@gmail.com

Citation:

Wagner, G. L., Hillier, A., Constantinou, N. C., Silvestri, S., Souza, A., Burns, K. J., et al. (2025). Formulation and calibration of CATKE, a one-equation parameterization for microscale ocean mixing. *Journal of Advances in Modeling Earth Systems*, 17, e2024MS004522. <https://doi.org/10.1029/2024MS004522>

Received 20 JUN 2024

Accepted 11 FEB 2025

Abstract We describe CATKE, a parameterization for fluxes associated with small-scale or “microscale” ocean turbulent mixing on scales between 1 and 100 m. CATKE uses a downgradient formulation that depends on a prognostic turbulent kinetic energy (TKE) variable and a diagnostic mixing length scale that includes a dynamic convective adjustment (CA) component. With its dynamic convective mixing length, CATKE predicts not just the depth spanned by convective plumes but also the characteristic convective mixing timescale, an important aspect of turbulent convection not captured by simpler static CA schemes. As a result, CATKE can describe the competition between convection and other processes such as shear-driven mixing and baroclinic restratification. To calibrate CATKE, we use Ensemble Kalman Inversion to minimize the error between 21 large eddy simulations (LESs) and predictions of the LES data by CATKE-parameterized single column simulations at three different vertical resolutions. We find that CATKE makes accurate predictions of both idealized and realistic LES compared to microscale turbulence parameterizations commonly used in climate models.

Plain Language Summary Turbulence is everywhere in the Earth’s ocean, from ephemeral swirls no bigger than a fingertip to gigantic eddies larger than Iceland. Ocean models used in climate studies simulate currents by dividing the ocean into grid cells between 10 and 100 km wide. As a result, ocean models do a decent job simulating eddies that are significantly larger than a single grid cell. But models do far worse at incorporating the effects of eddies that are person- to building-sized, which are smaller than a grid cell and therefore must be represented more approximately. This is a problem because these small yet mighty eddies mix heat and carbon deep into the ocean, and thus help keep the atmosphere from getting too hot, and too rich in CO₂. In this paper, we propose a new model component called “CATKE” (pronounced *kāt-kee*) that approximately incorporates the effect of small eddies in global ocean models. CATKE stands for “Convective Adjustment and Turbulent Kinetic Energy”, and keeps track of the *energy* of small-scale turbulence—a measure of how vigorous it is, and thus how much it mixes the ocean—to predict ocean mixing rates.

1. Introduction

Vertical mixing by “microscale” ocean turbulence, with scales between 1 and 100 m, is an important process affecting, for example, ocean uptake of atmospheric heat and carbon (Large et al., 1994; Omand et al., 2015; Price et al., 1986), the structure of the ocean interior (Luyten et al., 1983; Williams, 1991), and ocean circulation on decadal to millennial time-scales (Melet et al., 2022; Wunsch & Ferrari, 2004). In large-scale ocean models—from regional models covering tens of kilometers to global ocean models—microscale turbulent vertical fluxes are approximately modeled by parameterizations. Imperfect predictions by turbulence parameterizations contribute to biases in tropical sea surface temperature (SST) (G. Li & Xie, 2014), Southern Ocean boundary layer depth (DuVivier et al., 2018; Sallée et al., 2013), and water mass transformation rates (Groeskamp et al., 2019). These errors degrade the accuracy of climate projections that depend on accurate air-sea fluxes (sensitive to SST, Large et al., 1994) and the effective heat capacity of the upper ocean (which scales with the boundary layer depth, Gregory, 2000; Held et al., 2010).

This paper documents the development, calibration, and preliminary validation of a new parameterization for vertical mixing by ocean microscale turbulence. Our goal is to use the new parameterization in a GPU-based climate model that is automatically calibrated to observations, reports quantified uncertainties, and has an ocean component with $O(10\text{ km})$ or finer resolution that resolves ocean mesoscale turbulence. The dynamical

core of the GPU-based ocean component is described by Silvestri, Wagner, Constantinou, et al. (2024). In service of this ultimate goal, the work documented in this paper prioritizes not just accurate predictions, but also efficiency on Graphics Processing Units (GPUs) in high-resolution configurations. We also invest in automated calibration that constrains all of the parameterization's free parameters to 21 large eddy simulations (LESs) simultaneously, accounting for the peculiarities of our specific numerical implementation of the parameterization in a single column model. The 21 LES we use to calibrate and the additional 14 LES we use to validate the parameterization are described in Section 2. Uncertainty quantification, an important step for a future recalibration that leverages global-scale observations, is left for future work.

Our new parameterization, which we call “CATKE”, uses a downgradient formulation that estimates eddy diffusivities in terms of a prognostic turbulent kinetic energy (TKE) variable and a diagnostic mixing length with a novel dynamic CA component. CATKE is a “one-equation” model (because it includes an additional equation for TKE) that bears resemblance to a family of battle-tested parameterizations long used in European climate models (Blanke & Delecluse, 1993; Gaspar et al., 1990; Gutjahr et al., 2021; Jungclaus et al., 2022; Kuhlbrodt et al., 2018; Madec et al., 2017). One-equation downgradient parameterizations are appropriate for high-resolution ocean modeling and amenable to GPU performance optimization due to their spatially-local formulation. In contrast, the main feature of “*K*-profile” schemes used in many global ocean models—accommodating hours-long time steps (Reichl & Hallberg, 2018) by implicitly time-averaging mixing physics—does not benefit and may even degrade high-resolution simulations that resolve relatively fast mesoscale and submesoscale processes. Moreover, *K*-profile schemes achieve time-step flexibility by solving nonlinear algebraic equations for boundary layer depth (Large et al., 1994; Reichl & Hallberg, 2018; Reichl & Li, 2019), which may require significant optimization to achieve good performance on GPU-like systems (see by Zhang et al., 2020). As for two-equation “*k*– ϵ ”-type models (Canuto et al., 2001; Harcourt, 2015; Kantha & Clayson, 1994; Mellor & Yamada, 1982; Umlauf & Burchard, 2003), or equations with even more than two prognostic variables (Garanaik et al., 2024; Legay et al., 2024), CATKE is less expensive merely by having one fewer prognostic variable. CATKE therefore serves as a high-performance, well-calibrated “baseline” whose accuracy must be met or surpassed to justify the use of more expensive or more expressive parameterizations.

The downsides of downgradient parameterizations include unavoidable biases when non-local, non-downgradient fluxes dominate, such as during free convection (Large et al., 1994; Legay et al., 2024). We therefore devote special attention to free convection during CATKE's formulation, which is described in Section 3, to minimize this downgradient bias and assess its importance. Section 3.1.5 describes CATKE's diagnostic convective length scale and primary novelty, which uses dimensional analysis (Deardorff, 1970) to estimate a dynamically evolving convective diffusivity in terms of the local TKE. This improves upon constant “convective adjustment” diffusivities typically used with one-equation parameterizations in ocean climate models (typically $0.1 \text{ m}^2 \text{ s}^{-1}$; Madec et al., 2017; Gutjahr et al., 2021; Jungclaus et al., 2022), which cannot describe how the convective mixing rate *varies* with both boundary layer depth and the intensity of the destabilizing surface buoyancy flux. As a result, CATKE might be able to represent scenarios where mixing competes with other dynamics such as submesoscale restratification. We also implement different mixing lengths for momentum, tracer, TKE, and the TKE dissipation rate in shear-driven turbulence that all vary as a function of the local gradient Richardson number. This contrasts with typical approaches that estimate the TKE diffusivity as a constant multiple of the eddy viscosity (Blanke & Delecluse, 1993; Madec et al., 2017; Umlauf & Burchard, 2003), or which allow only the tracer mixing length to vary with Richardson number (Blanke & Delecluse, 1993; Madec et al., 2017).

CATKE's formulation could not be realized without an effective method for constraining CATKE's free parameters against observational or LES data. Section 4 describes how we use automatic, a posteriori calibration (Duraisamy, 2021; Frezat et al., 2022) to estimate CATKE's free parameters by minimizing the error between 21 variously-forced LES and the predictions of the LES data made by forward CATKE-parameterized single column simulations. Because a posteriori calibration computes errors based on simulated time-series, it can incorporate numerical errors that accumulate during time stepping and can leverage even indirect observational data if it can be computed from model output. For example, we leverage a posteriori calibration to specifically minimize CATKE's dependence on vertical resolution. We solve the calibration problem using Ensemble Kalman Inversion (EKI; see Iglesias et al., 2013), which does not require gradients of the error with respect to free parameters. We argue that automatic, EKI-based, a posteriori calibration is crucial not only for CATKE's development, but for

any parameterization development effort that seeks the simplest possible model that can adequately simulate available data. Without automatic calibration, we cannot generally tell whether bias has to do with structural error—which can only be addressed by formulation changes, possibly increasing model complexity—or because of poorly chosen parameters, which does not justify increasing model complexity.

We validate CATKE in various ways in Section 5. We first diagnose quantities with known physical interpretations such as CATKE's steady-state Richardson number and "similarity layer constant" (analogous to the von Kármán constant) in terms of CATKE's calibrated free parameters, and assess their consistency with values reported in the literature. Second, we compare CATKE's predictions versus idealized LES, both including those used in calibration and additional LES that are more strongly and more weakly forced than the calibration cases. In this way we test whether CATKE can reproduce the training data as well as CATKE's capacity for extrapolation. Third, we compare CATKE predictions to LES of a long 34-day deep cycle turbulence case, which is forced by realistic winds, heat fluxes, salinity fluxes, solar insolation, and lateral flux divergences derived from a regional ocean model (Whitt et al., 2022). This case illustrates CATKE's ability to extrapolate to cases with time-dependent forcing. Fourth, we evaluate the sensitivity of CATKE's predictions to vertical resolution and time-step size. After finding that CATKE can be sensitive to time steps longer than 1 min if the forcing is very strong and the vertical resolution is 1 m or finer, we describe a split-explicit substepping scheme for TKE that nearly eliminates time step sensitivity while preserving the ability to step forward momentum and tracers with a relatively long time step.

We also compare CATKE to the K -profile parameterization (KPP; Large et al., 1994) and a second-moment closure for Langmuir turbulence (Langmuir turbulence second moment closure (SMC-LT), or "SMC-LT"; Harcourt, 2015), which are implemented in the General Ocean Turbulence Model (GOTM; see Umlauf & Burchard, 2005; Q. Li et al., 2019). CATKE outperforms both in almost all cases—though the results must be taken with a grain of salt, because both KPP and SMC-LT have been calibrated to different data. Despite this caveat, the comparison contributes context to CATKE's small but finite biases versus constant forcing LES.

In Section 6, we conclude with a discussion about future efforts to calibrate CATKE against more comprehensive data sets, and model development efforts to capture physics not considered in this work, such as the effect of surface wave fields that vary independently from winds and the modulation of turbulence by lateral density fronts. The most important piece of future work is the construction of a global calibration context to further refine CATKE's free parameters using satellite and in-situ ocean observations.

2. Large Eddy Simulations of Turbulent Mixing Beneath Surface Waves

We begin by defining the parameterization problem that drives the cyclical process of formulating, calibrating, and validating CATKE. In this paper, the parameterization problem is posed by comparing high-fidelity and three-dimensional LESs of turbulent mixing with one-dimensional parameterized models for the horizontally-averaged dynamics of the LES. Our LES integrate the rotating, wave-averaged Boussinesq equations simplified for a steady surface wave field (Craig & Leibovich, 1976; Huang, 1979; Suzuki & Fox-Kemper, 2016),

$$\partial_t \mathbf{U}^L + (\mathbf{U}^L \cdot \nabla) \mathbf{U}^L + (f \hat{\mathbf{z}} - \nabla \times \mathbf{U}^S) \times \mathbf{U}^L + \nabla P = B \hat{\mathbf{z}} + \partial_t \mathbf{U}^S + \mathbf{F}_u, \quad (1)$$

$$\nabla \cdot \mathbf{U}^L = 0, \quad (2)$$

$$\partial_t C + (\mathbf{U}^L \cdot \nabla) C = -\nabla \cdot \mathbf{J}_c + F_c, \quad (3)$$

where $\mathbf{U}^L = (U^L, V^L, W^L)$ is the Lagrangian-mean velocity, \mathbf{U}^S is the Stokes drift associated with surface waves (which are always steady and oriented in the $\hat{\mathbf{x}}$ -direction in this paper), P is Eulerian-mean kinematic pressure, B is Eulerian-mean buoyancy, f is the Coriolis parameter, \mathbf{F}_u is a momentum forcing term representing surface wind stress, C is any tracer such as temperature or salinity, and F_c is forcing term for C representing boundary conditions, solar insolation, and other imposed body forcing. The Lagrangian-mean velocity \mathbf{U}^L is defined as the sum of the Eulerian-mean velocity and Stokes drift, and setting $\mathbf{U}^S = 0$ reduces Equation 1 to the ordinary Navier–Stokes equations. Note that we have neglected molecular diffusion from Equations 1 and 3, as well as diffusion by a hypothetical LES closure, to simplify the ensuing discussion. In this work we use buoyancy B itself as a tracer, which is tantamount to using a linear equation of state with a single constituent.

We conduct 35 LES of 1–3 forced by constant, horizontally-uniform fluxes of momentum and buoyancy in a $512 \text{ m} \times 512 \text{ m} \times 256 \text{ m}$ horizontally-periodic domain with $O(1 \text{ m})$ resolution using Oceananigans (Ramadhan et al., 2020; Wagner et al., 2025). Grid-scale dissipation of kinetic energy and tracer variance is implicitly provided by a Weighted, Essentially Non-Oscillatory (WENO, Shu, 2020) advection scheme. The advantages of this approach are described by Pressel et al. (2017). All 35 LES are initialized with the same piecewise-constant density stratification given in Equation A1, which has a weakly-stratified near-surface layer, a more strongly stratified middle layer, and a weakly-stratified lower layer. The surface momentum flux or “wind stress” τ_x is defined via F_u in 1 as

$$F_u = -\partial_z [\tau_x H(z)] \hat{x}, \quad \text{where} \quad H(z) \stackrel{\text{def}}{=} \begin{cases} 1 & \text{if } z \geq 0 \\ 0 & \text{if } z < 0 \end{cases} \quad (4)$$

is a Heaviside function. Negative stress $\tau_x < 0$ forces a current in the $+x$ -direction. Two types of buoyancy fluxes are used: a destabilizing surface flux $J_b > 0$ representing cooling or heat loss, which is defined via F_b in Equation 3 via

$$F_b = -\partial_z [J_b H(z)]. \quad (5)$$

We also include 5 LES forced by both wind stress and stabilizing buoyancy forcing that represents heating by solar insolation. In these “sunny” cases, the flux divergence of buoyancy F_b is given by

$$F_b = -\partial_z I, \quad \text{where} \quad I(z) = J_b [\epsilon_1 e^{z/\lambda_1} + (1 - \epsilon_1) e^{z/\lambda_2}]. \quad (6)$$

In 6, $I(z)$ is the buoyancy flux profile associated with penetrating solar insolation, $J_b < 0$ is the surface solar insolation, ϵ_1 is the fraction of penetrating radiation absorbed over the vertical scale λ_1 , and $(1 - \epsilon_1)$ is the remaining fraction absorbed over λ_2 . All simulations use $\epsilon_1 = 0.6$, $\lambda_1 = 1 \text{ m}$, and $\lambda_2 = 16 \text{ m}$ (see for example the solar insolation used by Whitt et al., 2022).

The LES are organized by duration into 6-, 12-, 24-, 48-, and 72-hr “suites”. Because all the LES are initialized identically and run until the boundary layer is roughly half the depth of the domain, duration indicates forcing strength: the 6-hr-suite are the most strongly forced and the 72-hr suite simulations are the most weakly forced. So that we can validate CATKE’s ability to extrapolate outside the training data set, only intermediately-forced 12-, 24-, and 48-hr suites are used for calibration. The 35 LES are divided into 5 “suites” with 7 cases each, according to their duration and the intensity of the surface fluxes: the 6-hr suite exhibits extreme forcing, while the 72-hr suite exhibits relatively weak forcing. Each suite consists of 7 physical scenarios that represent different forcing regimes:

- “free convection”, which has pure destabilizing buoyancy forcing and no winds,
- “weak wind strong cooling”,
- “medium wind medium cooling”,
- “strong wind weak cooling”,
- “strong wind”, with no buoyancy forcing,
- “strong wind no rotation” with no buoyancy forcing and $f = 0$.
- “strong wind and sunny” with penetrative heating, wind forcing, and $f = 0$.

The “strong wind no rotation” and “strong wind and sunny” are non-rotating with $f = 0$, and the rest are rotating with Coriolis parameter $f = 10^{-4} \text{ s}^{-1}$. The range of buoyancy fluxes roughly corresponds to cooling between $156\text{--}2,000 \text{ W m}^{-2}$ or heating by penetrating solar insolation between $104\text{--}1,250 \text{ W m}^{-2}$, and the momentum fluxes correspond to 10-m atmospheric winds of approximately $9\text{--}25 \text{ m s}^{-1}$ and oriented in the \hat{x} -direction. The fluxes associated with each case are summarized in Tables 1 and 2.

In any LES with wind forcing, we also include the effect of wind-driven surface waves through an estimate of $\partial_z U^S = \partial_z U^S \hat{x}$ in 1 for equilibrium waves (Lenain & Pizzo, 2020). The equilibrium wave model depends on the peak wavenumber of the surface wave field, which is chosen so that the Langmuir number La is

Table 1
Summary of Surface Boundary Conditions for Large Eddy Simulations (LES) Used to Calibrate CATKE

Suite	Case	J_b ($\text{m}^2 \text{s}^{-3}$)	$ \tau_x $ ($\text{m}^2 \text{s}^{-2}$)	Q ($\frac{\text{W}}{\text{m}^2}$)	u_{10} ($\frac{\text{m}}{\text{s}}$)
12 hr	Free convection	$+4.8 \times 10^{-7}$	0	+1000	0
12 hr	Weak wind strong cooling	$+4.0 \times 10^{-7}$	4.0×10^{-4}	+833	15
12 hr	Mid wind mid cooling	$+3.2 \times 10^{-7}$	6.0×10^{-4}	+667	17
12 hr	Strong wind weak cooling	$+2.0 \times 10^{-7}$	8.0×10^{-4}	+417	20
12 hr	Strong wind	0	9.0×10^{-4}	0	21
12 hr	Strong wind no rotation	0	6.0×10^{-4}	0	17
12 hr	Strong wind and sunny	-5.0×10^{-7}	9.0×10^{-4}	-1042	21
24 hr	Free convection	$+2.4 \times 10^{-7}$	0	+500	0
24 hr	Weak wind strong cooling	$+2.0 \times 10^{-7}$	3.0×10^{-4}	+417	13
24 hr	Mid wind mid cooling	$+1.6 \times 10^{-7}$	4.5×10^{-4}	+333	16
24 hr	Strong wind weak cooling	$+1.0 \times 10^{-7}$	5.9×10^{-4}	+208	17
24 hr	Strong wind	0	6.8×10^{-4}	0	18
24 hr	Strong wind no rotation	0	3.0×10^{-4}	0	13
24 hr	Strong wind and sunny	-3.0×10^{-7}	4.5×10^{-4}	-625	16
48 hr	Free convection	$+1.2 \times 10^{-7}$	0	+250	0
48 hr	Weak wind strong cooling	$+1.0 \times 10^{-7}$	2.0×10^{-4}	+208	11
48 hr	Mid wind mid cooling	$+8.0 \times 10^{-8}$	3.4×10^{-4}	+167	14
48 hr	Strong wind weak cooling	$+5.0 \times 10^{-8}$	3.8×10^{-4}	+104	15
48 hr	Strong wind	0	4.5×10^{-4}	0	16
48 hr	Strong wind no rotation	0	1.6×10^{-4}	0	10
48 hr	Strong wind and sunny	-1.0×10^{-7}	2.0×10^{-4}	-208	11

Note. All LES are initialized with the buoyancy profile described in Equation A1 and use the traditional f -plane approximation with Coriolis parameter $f = 10^{-4} \text{ s}^{-1}$, except “strong wind no rotation” and “strong wind and sunny”, which omit Coriolis forces entirely. The “suite” indicates simulation duration. J_b is the surface buoyancy flux, τ_x is the kinematic momentum flux (momentum flux divided by ocean reference density), $Q \approx \rho_o c_p J_b / (\alpha g)$ is the heat flux associated with J_b , and u_{10} is an estimate of the 10-m wind speed associated with τ_x according to Equation A5 using reference density $\rho_o = 1024 \text{ kg m}^{-3}$, seawater heat capacity $c_p = 3991 \text{ J } ^\circ\text{C}^{-1}$, thermal expansion coefficient $\alpha = 2 \times 10^{-4} \text{ } ^\circ\text{C}^{-1}$, gravitational acceleration $g = 9.81 \text{ m s}^{-2}$ are used for Q and u_{10} . When the surface buoyancy flux is negative ($J_b < 0$), J_b represents $J_b = I(z = 0)$, where $I(z)$ is the buoyancy flux associated with penetrating solar insolation in Equation 6. The forcing in Equation 3 is then defined as $F_b = -\partial_z I$. All fluxes use the convention that a positive flux carries quantities upwards, out of the ocean, which means a negative τ_x drives currents in the $+\hat{x}$ direction and a positive buoyancy flux cools the ocean by extracting buoyancy. Additional LES used to validate CATKE are summarized in Table 2.

$$La \stackrel{\text{def}}{=} \sqrt{\frac{u_\star}{U^S(z=0)}} \approx 0.3, \quad (7)$$

close to the peak of its global distribution (Belcher et al., 2012). In 7, u_\star is the friction velocity computed from the surface wind stress (here $u_\star = \sqrt{|\tau_x|}$, where $\tau = \tau_x \hat{x}$ is the wind stress). All LES are initialized from rest with $U^L = 0$. The LES also include a forced passive tracer, providing additional information about the time scales of mixing in the interior of the boundary layer. The initial density stratification, numerical methods, Stokes drift model, effects of including Stokes drift, and the sensitivity of the LES to resolution are described in Appendix A. Out of the 35 LES cases, 21 are used for calibration, while another 14 are reserved for validation. Figure 1 visualizes vertical velocity in 9 of the 35 cases.

Table 2

Summary of Surface Boundary Conditions for LES Used to Validate CATKE

Suite	Case	J_b ($\text{m}^2 \text{s}^{-3}$)	$ \tau_x $ ($\text{m}^2 \text{s}^{-2}$)	Q ($\frac{\text{W}}{\text{m}^2}$)	u_{10} ($\frac{\text{m}}{\text{s}}$)
6 hr	Free convection	$+9.6 \times 10^{-7}$	0	+2000	0
6 hr	Weak wind strong cooling	$+8.0 \times 10^{-7}$	5.0×10^{-4}	+1666	16
6 hr	Mid wind mid cooling	$+6.4 \times 10^{-7}$	8.0×10^{-4}	+1333	20
6 hr	Strong wind weak cooling	$+4.0 \times 10^{-7}$	1.2×10^{-3}	+833	23
6 hr	Strong wind	0	1.4×10^{-3}	0	24
6 hr	Strong wind no rotation	0	1.1×10^{-3}	0	22
6 hr	Strong wind and sunny	-6.0×10^{-7}	1.5×10^{-3}	-1250	25
72 hr	Free convection	$+8.7 \times 10^{-8}$	0	+181	0
72 hr	Weak wind strong cooling	$+7.5 \times 10^{-8}$	1.8×10^{-4}	+156	11
72 hr	Mid wind mid cooling	$+6.0 \times 10^{-8}$	2.9×10^{-4}	+125	13
72 hr	Strong wind weak cooling	$+3.8 \times 10^{-8}$	3.4×10^{-4}	+79	14
72 hr	Strong wind	0	4.1×10^{-4}	0	15
72 hr	Strong wind no rotation	0	1.1×10^{-4}	0	9
72 hr	Strong wind and sunny	-5.0×10^{-8}	1.3×10^{-4}	-104	9

Note. See Table 1 for a description and a summary of the LES used to calibrate CATKE.

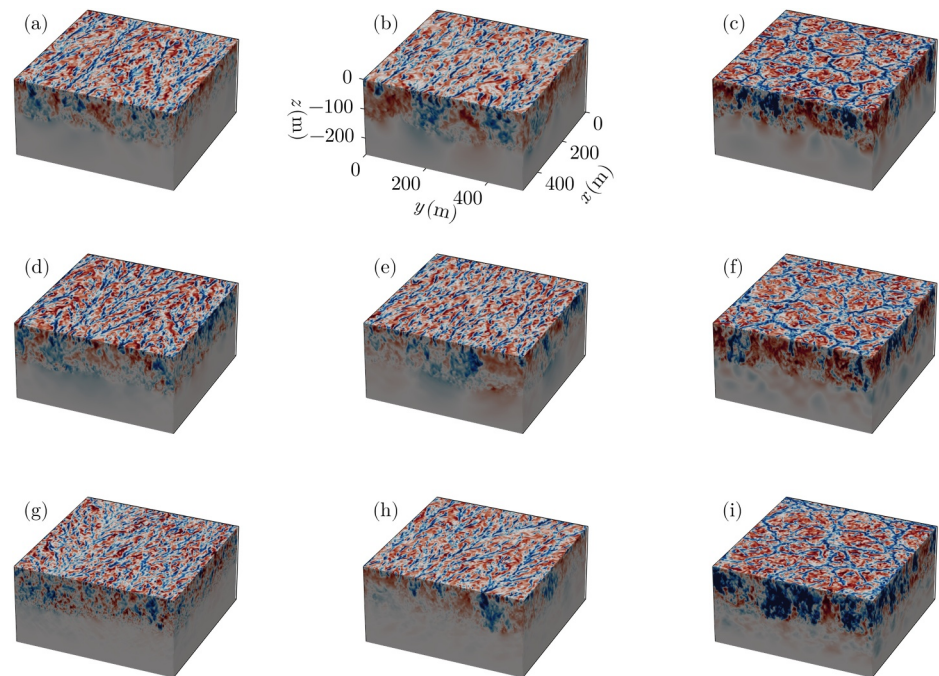


Figure 1. Visualization of vertical velocity w in 9 of 35 large eddy simulations (LESs) of the ocean surface boundary layer used in this paper, forced variously by winds, surface waves, and heat fluxes. All LES, which are summarized in Tables 1 and 2 and described in more detail in Appendix A, are initialized with the same density stratification. (a)–(c) show strongly-forced LES after just 6 hr of simulation, (d)–(f) show LES driven by medium-strength forcing after 24 hr, and (g)–(i) show weakly forced LES after 72 hr (a), (d), and (g) show a purely wind and wave driven case, (b), (e), and (h) are forced by a mixture of winds, waves, and cooling, and (c), (f), and (i) are “free convection” cases forced only by cooling with no winds and waves. All simulations are rotating with Coriolis parameter $f = 10^{-4} \text{ s}^{-1}$. The colorscale for each panel saturates at $\frac{1}{2} \max|w|$. For each panel, $\max|w|$ is (a) 0.26, (b) 0.29, (c) 0.086, (d) 0.20, (e) 0.23, (f) 0.070, (g) 0.056, (h) 0.14, and (i) 0.041 m s^{-1} .

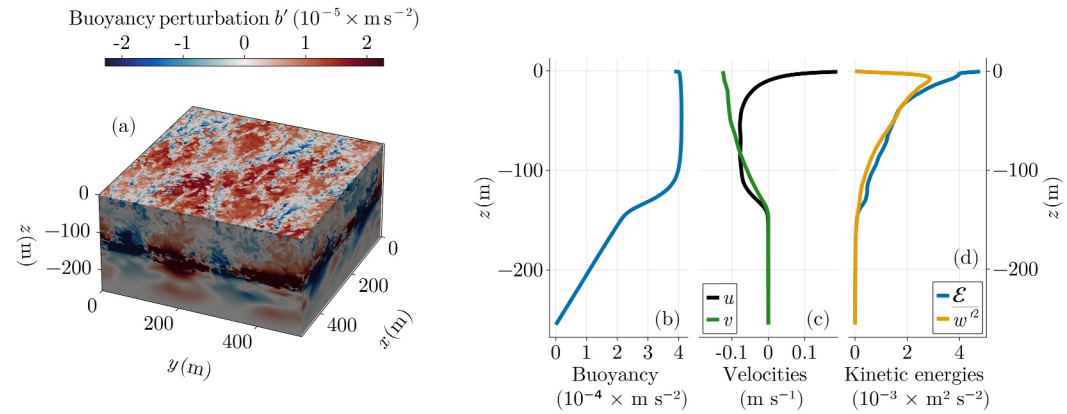


Figure 2. Illustration of horizontally-averaged data from the 12-hr strong wind, weak cooling LES. Panel (a) shows the buoyancy perturbation b' . Note the colorbar is strongly saturated to illustrate boundary layer structure; the buoyancy perturbation is particularly large at the base of the boundary layer, where the horizontally-averaged buoyancy gradient is also strong. (b) Shows the horizontally-averaged buoyancy b , (c) shows the horizontally-averaged velocities u, v , and (d) shows the horizontally-averaged fluctuation kinetic energy, $\mathcal{E} \stackrel{\text{def}}{=} (\overline{u'^2} + \overline{v'^2} + \overline{w'^2})/2$ and horizontally-averaged vertical velocity variance, $\overline{w'^2}$.

2.1. The Single Column Context

We would like to develop a model that can predict the horizontally-averaged momentum and buoyancy simulated by the LES. We therefore decompose all three-dimensional variables Ψ in 1–3 into a horizontally-averaged component $\psi \stackrel{\text{def}}{=} \overline{\Psi}$ and a fluctuation ψ' such that,

$$\Psi(x, y, z, t) = \underbrace{\overline{\Psi}(z, t)}_{\stackrel{\text{def}}{=} \psi(z, t)} + \psi'(x, y, z, t), \quad (8)$$

where the overline $\overline{(\cdot)}$ denotes a horizontal average, and $\Psi \in (U^L, V^L, W^L, C)$ includes the velocity components U^L, V^L, W^L , and tracer concentrations C . Note that the horizontal average of 2 and the horizontal homogeneity of our LES implies that $w^L = 0$ and $W^L = w'$ and thus the vertical momentum equation reduces to a statement of wave-modified hydrostatic balance. Figure 2 shows horizontally-averaged buoyancy, velocity, and kinetic energy profiles alongside a three-dimensional visualization of the buoyancy perturbation b' for the 12-hr strong wind, weak cooling case.

Next, we derive a set of equations that governs the horizontally-averaged zonal momentum $u(z, t)$, meridional momentum $v(z, t)$, and any tracer $c(z, t)$ by taking a horizontal average of 1 and 3 to obtain,

$$\partial_t u - f v = -\partial_z \overline{w' u'} + \bar{F}_u, \quad (9)$$

$$\partial_t v + f u = -\partial_z \overline{w' v'} + \bar{F}_v, \quad (10)$$

$$\partial_t c = -\partial_z \overline{w' c'} + \bar{F}_c, \quad (11)$$

where u, v represent the horizontal average of the horizontal Lagrangian-mean velocities U^L, V^L , and the superscript L is omitted to simplify notation. Lateral fluxes vanish from 9–11 due to horizontal homogeneity. No Stokes-drift-dependent terms enter into 9–11 because $U^S(z)$ is horizontally uniform. Figure 2 illustrates the horizontally-averaged buoyancy, velocity, and TKE for the 12-hr strong wind, weak cooling case.

The parameterization problem may now be stated: we seek a parameterization that predicts the vertical fluxes $\overline{w' u'}$, $\overline{w' v'}$, and $\overline{w' c'}$ in terms of the resolved state u, v, c , boundary conditions, and potentially, additional auxiliary variables. For example, the parameterization described in the next section uses a downgradient formulation $\overline{w' c'} \sim \partial_z c$ to predict vertical tracer and momentum fluxes.

2.2. Connection to the Regional and Global Ocean Modeling Context

Our LES, and the models that predict the horizontal average of the LES, may be described as “single column models”. This nomenclature reflects the notion that the models simulate the vertical redistribution of momentum and tracers by turbulent motions in a single column of a three-dimensional ocean model. Indeed, we envision that the single column context is generalized to a large-scale ocean simulation merely by adding advection by motions somewhat larger than the scale of the LES domain. This approach relies on two key assumptions. First, the microscale turbulence must be horizontally homogeneous so as to ignore lateral flux divergences. Second, there must be a scale separation between microscale turbulence and larger-scale motions so that interactions between the two can be ignored.

For typical oceanic situations, the first assumption is likely satisfied because vertical gradients are much larger than horizontal ones on the scales of a “single column model” and thus the vertical flux divergences dominate over horizontal divergences. In other words the ocean is more homogeneous in the horizontal than in the vertical on scales of $O(100\text{ m})$. The second assumption is more problematic especially near the ocean surface and bottom boundaries. While microscale turbulence does not significantly interact with mesoscale geostrophic eddies with scales of $O(10\text{--}100\text{ km})$, there is growing evidence of interactions between submesoscale frontal dynamics with scales of $O(100\text{ m--}10\text{ km})$ and microscale turbulence (see reviews by Thomas et al., 2008; McWilliams, 2016; J. R. Taylor & Thompson, 2023). Frontal instabilities are also effective at restratifying the ocean boundary layers during time of weak microscale turbulence (see for example Boccaletti et al., 2007). These interactions are presently ignored in the formulation of microscale turbulence parameterizations, but they are an obvious direction for future development of CATKE. Following the approach outlined in this paper, such an effort will require generating a library of simulations which resolve microscale turbulence in the presence of ocean fronts, extending CATKE to include those physics, and then calibrating the extended CATKE against the new library of those simulations.

Similarly, microscale turbulent mixing in the ocean interior requires considering multiscale dynamics. For example, internal waves generated by surface winds and tide-bathymetry interactions produce a direct cascade of internal wave energy to progressively smaller scales until wave breaking finally transfers energy to microscale turbulence. Incorporating the physics of turbulent mixing driven by internal wave breaking is another area for future development.

3. CATKE Formulation

CATKE models the horizontally-averaged vertical fluxes $\overline{w'\psi'}$ appearing on the right side of 9–11 with a downgradient, mixing length formulation (Prandtl et al., 1925),

$$\overline{w'\psi'} \approx - \underbrace{\ell_\psi \sqrt{e}}_{\stackrel{\text{def}}{=} K_\psi} \partial_z \psi, \quad (12)$$

where e is the TKE, \sqrt{e} is the turbulent velocity scale, and ℓ_ψ is the mixing length for the horizontally-averaged variable $\psi(z, t)$. After choosing to parameterize turbulent transport with eddy diffusion that depends on the turbulent velocity \sqrt{e} and mixing length ℓ_ψ , the form $K_\psi = \ell_\psi \sqrt{e}$ follows from dimensional analysis. CATKE invokes three mixing lengths and three eddy diffusivities for horizontal velocities (ℓ_u and K_u), tracers (ℓ_c and K_c), and TKE (ℓ_e and K_e).

With 12, the single column equations become

$$\partial_t u - fv = \partial_z (K_u \partial_z u) + \bar{F}_u, \quad (13)$$

$$\partial_t v + fu = \partial_z (K_u \partial_z v) + \bar{F}_v, \quad (14)$$

$$\partial_t c = \partial_z (K_c \partial_z c) + \bar{F}_c. \quad (15)$$

In this paper we use a linear equation of state that relates density to a single thermodynamic constituent, such that the buoyancy b is just another tracer,

$$\partial_t b = \partial_z (K_c \partial_z b) + \bar{F}_b. \quad (16)$$

The buoyancy gradient $N^2 \stackrel{\text{def}}{=} \partial_z b$ appears in many of the scaling arguments central to CATKE's formulation, where N is often referred to as the “buoyancy frequency”. Note that in more realistic simulations of seawater, b and N^2 are functions of geopotential height, mean temperature, and mean salinity through the empirically-determined seawater equation of state (McDougall & Barker, 2011).

Next we turn to the estimation of the TKE e , and thus the turbulent velocity scale \sqrt{e} in 12. For this we first introduce the kinetic energy of the subgrid velocity field, \mathcal{E} , defined in terms of the velocity fluctuations (u', v', w') ,

$$\mathcal{E} \stackrel{\text{def}}{=} \frac{1}{2} \overline{|u'|^2} = \frac{1}{2} (\overline{u'^2} + \overline{v'^2} + \overline{w'^2}). \quad (17)$$

We postulate a close relationship between e in 12 and the subgrid kinetic energy, \mathcal{E} . However, this is a relationship rather than an identity, because \mathcal{E} has contributions from motions that are unrelated to the eddy diffusivity in 12. For example, internal waves generated by convective plumes make a significant contribution to \mathcal{E} below the base of boundary layer, despite that there is no mixing there. Moreover, even if the kinetic energy and mixing length are known, a correlation coefficient is still required to compute the eddy diffusivity in 12 (G. I. Taylor, 1922). We therefore interpret e as a *latent variable* whose sole purpose is to enable accurate computation of the eddy diffusivity in 12, rather conflating e with the observable but less relevant quantity \mathcal{E} . This interpretation has implications for calibration: we do not use discrepancy between LES-derived \mathcal{E} and e to constrain CATKE's free parameters. Instead, we only use the discrepancies between LES and model-predicted variables u , v , and c . CATKE's e is therefore free to deviate from \mathcal{E} if this produces more accurate eddy diffusivities and thus more accurate predictions of u , v , c . Interpreting e as a latent variable rather than as the subgrid kinetic energy \mathcal{E} is also proposed by Kolmogorov (see Spalding, 1991) and Saffman (1970).

Though we define e as a latent variable, we still expect similarity between e and \mathcal{E} on physical grounds—where there is turbulence, there will be mixing—and following prior work (Gaspar et al., 1990; Saffman, 1970; Spalding, 1991; Umlauf & Burchard, 2003), use the evolution equation for \mathcal{E} to formulate a model for the evolution of e . An equation describing the evolution of \mathcal{E} can be derived from 1, including the molecular stress divergence $\nu \nabla^2 (U^L - U^S)$ (we include the Stokes drift term here for completeness, though it does not contribute to the equation for \mathcal{E}). The result is

$$\partial_t \mathcal{E} = \underbrace{-\partial_z (\overline{w' \mathcal{E}'} + \overline{w' p'}) - \nu \partial_z \mathcal{E}}_{\text{transport}} - \underbrace{\overline{u' w'} \cdot \partial_z \mathbf{u}}_{\text{shear production}} + \underbrace{\overline{w' b'}}_{\text{buoyancy flux}} - \underbrace{\nu \overline{|\nabla \mathbf{u}'|^2}}_{\text{dissipation}}, \quad (18)$$

where ν is the kinematic viscosity, p is kinematic pressure (dynamic pressure divided by a reference density) and $\mathcal{E}' = \frac{1}{2} |\mathbf{u}'|^2 - \mathcal{E}$. Because \mathbf{u} is the horizontally-averaged Lagrangian-mean velocity, the shear production term in 18 represents the total transfer of kinetic energy from the average \mathbf{u} to the fluctuations \mathbf{u}' , including the so-called “Stokes production” term (McWilliams et al., 1997). Again following prior work (Gaspar et al., 1990; Saffman, 1970; Spalding, 1991; Umlauf & Burchard, 2003) we write the equation for e using terms that mirror each term in Equation 18:

$$\partial_t e = \underbrace{\partial_z (K_e \partial_z e)}_{\text{transport}} + \underbrace{K_u |\partial_z \mathbf{u}|^2}_{\text{shear production}} - \underbrace{K_c N^2}_{\text{buoyancy flux}} - \underbrace{\frac{e^{3/2}}{\ell_D}}_{\text{dissipation}}, \quad (19)$$

where $|\partial_z \mathbf{u}|^2 = (\partial_z u)^2 + (\partial_z v)^2$ is the square vertical shear of the horizontally-averaged velocity field \mathbf{u} ($w = 0$ because of horizontal homogeneity), K_e is the vertical diffusivity of e , ℓ_D is the “dissipation length scale”, and we have labeled the corresponding terms in 18 and 19. The shear production and buoyancy flux terms are formulated by applying the eddy diffusivity hypothesis (12) to their corresponding expressions in Equation 18. Like in the

budget for \mathcal{E} , the shear production term in 19 represents the total shear production including both “Eulerian” and “Stokes” production.

Even with perfect predictions of u, v, c —and therefore perfect shear production and buoyancy flux— \mathcal{E} and e can still differ because of the approximate transport and dissipation terms in 19. In particular, we assume in 19 that the transport of e , which helps to deepen boundary layers by modeling turbulence spreading away from turbulence-generating regions, can be modeled with an eddy diffusivity $K_e = \ell_e \sqrt{e}$. To model the dissipation of e we introduce the dissipation length scale ℓ_D , which has a similar form to the mixing lengths ℓ_u, ℓ_c , and ℓ_e . The expression $e^{3/2}/\ell_D$ in 19 follows on dimensional grounds.

Equation 19 requires boundary conditions. We impose a no-flux condition on e at the bottom. (Extending CATKE to describe the bottom boundary layer in the future may require imposing a different bottom boundary condition.) At $z = 0$, we parameterize subgrid production of e by wind stress and destabilizing buoyancy fluxes across the uppermost cell interface with

$$J_e^{\text{def}} = -K_e \partial_z e|_{z=0} = -\mathbb{C}_J^{\text{shear}} u_\star^3 - \mathbb{C}_J^{\text{conv}} w_\Delta^3, \quad \text{where} \quad w_\Delta^3 \stackrel{\text{def}}{=} \Delta z \max(J_b, 0), \quad (20)$$

and $\mathbb{C}_J^{\text{shear}}$ and $\mathbb{C}_J^{\text{conv}}$ are constant, non-dimensional free parameters, J_b is the surface buoyancy flux defined such that $J_b > 0$ removes buoyancy and thus causes convection, Δz is the distance between the top of the ocean domain and the first interior cell interface, and w_Δ^2 is the convective TKE scale that follows from a balance between buoyant production and dissipation estimated using the grid spacing Δz as a length scale. u_\star in 20 is the ocean-side friction velocity,

$$u_\star \stackrel{\text{def}}{=} (\tau_x^2 + \tau_y^2)^{1/4}, \quad (21)$$

defined in terms of the zonal and meridional kinematic momentum fluxes τ_x and τ_y (wind stresses divided by reference water density). Note that other TKE-based models (Blanke & Delecluse, 1993; Madec et al., 2017) prescribe surface TKE (rather than TKE flux), and do not depend on the surface buoyancy flux J_b .

Equation 20 introduces the notation

$$\mathbb{C}_{\text{component}}^{\text{label}} \quad (22)$$

For two free parameters $\mathbb{C}_J^{\text{shear}}$ and $\mathbb{C}_J^{\text{conv}}$, where “label” indicates the parameter’s role and “component” associates the parameter with a variable or model component.

3.1. Turbulence Length Scale Model

We decompose the four length scales $\ell_\psi \in (\ell_u, \ell_c, \ell_e, \ell_D)$ into a shear-dominated length scale ℓ_ψ^{shear} limited by density-stratification and surface distance, and a convection-dominated length scale ℓ_ψ^{conv} limited by the depth of the convective boundary layer. At any time and location, the maximum of these two length scales is chosen as the mixing length via

$$\ell_\psi = \max(\ell_\psi^{\text{conv}}, \ell_\psi^{\text{shear}}), \quad (23)$$

encapsulating a sharp separation between turbulence regimes. We next describe a length scale formulation that can be calibrated to predict turbulent fluxes associated with the kinds of flows plotted in Figure 1.

3.1.1. Shear Turbulence Length Scale

To represent shear-dominated turbulence, we use the length scale

$$\ell_\psi^{\text{shear}} = \mathbb{S}_\psi(Ri) \min\left(\frac{\sqrt{e}}{N_+}, \mathbb{C}_s^s d\right), \quad \text{where} \quad N_+^2 \stackrel{\text{def}}{=} \max(0, \partial_z b) \quad (24)$$

with d the distance to the ocean surface, \mathbb{C}^s a free parameter (“s” for “surface”), and \mathbb{S}_ψ a “stability function” defined below. \sqrt{e}/N is the vertical distance traversed by a patch of turbulence expending all its kinetic energy e to mix the uniform stratification N . Blanke and Delecluse (1993) point out that \sqrt{e}/N is a local approximation to the more complete but computationally-expensive length scale proposed by Gaspar et al. (1990).

We use (24) for $\mathcal{C}_c^{\text{shear}}$, $\mathcal{C}_u^{\text{shear}}$, and $\mathcal{C}_e^{\text{shear}}$. For the dissipation length scale $\mathcal{D}^{\text{shear}}$, we use

$$\mathcal{D}^{\text{shear}} = \frac{1}{\mathbb{S}_D(Ri)} \min\left(\frac{\sqrt{e}}{N_+}, \mathbb{C}^s d\right), \quad (25)$$

so that the stability function for the dissipation length scale is $1/\mathbb{S}_D$. The alternative formulation in 25 yields a tight connection between \mathbb{S}_D ’s free parameters and e dissipation, and facilitates the physical interpretation of CATKE’s parameters.

The stability functions $\mathbb{S}_\psi(Ri)$ and $1/\mathbb{S}_D(Ri)$ in 24 and 25 depend on the gradient Richardson number,

$$Ri \stackrel{\text{def}}{=} \frac{\partial_z b}{|\partial_z \mathbf{u}|^2}, \quad (26)$$

which means that each diffusivity K_ψ also depends explicitly on Ri . More specifically, we hypothesize that K_u , K_c , and K_e are all explicit functions of $|\partial_z \mathbf{u}|^2$ in addition to N^2 , e , and the wall-distance d . CATKE is therefore more expressive than the closure described by Blanke and Delecluse (1993), wherein K_u and K_e do not depend explicitly on $|\partial_z \mathbf{u}|^2$. Second-moment closures also define K_u and K_c that depend on $|\partial_z \mathbf{u}|^2$, in addition to N^2 , e , and the dissipation rate ϵ (see, for example Burchard & Bolding, 2001). Ri -dependent stability functions also allow CATKE to capture, in some form, the well-known dependence between Ri and the turbulent Prandtl number (D. Li, 2019; C. Caulfield, 2021)

$$Pr(Ri) \stackrel{\text{def}}{=} \frac{K_u}{K_c} = \frac{\mathbb{S}_u(Ri)}{\mathbb{S}_c(Ri)}. \quad (27)$$

We balance expressiveness and parsimony with four-part $\mathbb{S}_\psi(Ri)$,

$$\mathbb{S}_\psi(Ri) = \begin{cases} \mathbb{C}_\psi^- & \text{when } Ri < 0, \\ \mathbb{C}_\psi^0 & \text{when } 0 \leq Ri \leq \mathbb{C}_{Ri}^0, \\ \mathbb{C}_\psi^0 + (\mathbb{C}_\psi^\infty - \mathbb{C}_\psi^0) \frac{Ri - \mathbb{C}_{Ri}^0}{\mathbb{C}_{Ri}^\delta - Ri} & \text{when } \mathbb{C}_{Ri}^0 < Ri < \mathbb{C}_{Ri}^0 + \mathbb{C}_{Ri}^\delta, \\ \mathbb{C}_\psi^\infty & \text{when } Ri \geq \mathbb{C}_{Ri}^0 + \mathbb{C}_{Ri}^\delta. \end{cases} \quad (28)$$

in 28, the parameter \mathbb{C}_{Ri}^0 is the “transition Ri ”. The four regions of the stability function are:

- Constant $\mathbb{S}_\psi = \mathbb{C}_\psi^-$ for unstably-stratified shear turbulence with $Ri < 0$.
- Constant $\mathbb{S}_\psi = \mathbb{C}_\psi^0$ for near-neutral turbulence with $0 \leq Ri \leq \mathbb{C}_{Ri}^0$.
- Linearly-varying from \mathbb{C}_ψ^0 to \mathbb{C}_ψ^∞ as Ri increases from \mathbb{C}_{Ri}^0 to $\mathbb{C}_{Ri}^0 + \mathbb{C}_{Ri}^\delta$.
- Constant $\mathbb{S}_\psi = \mathbb{C}_\psi^\infty$ when high $Ri > \mathbb{C}_{Ri}^0 + \mathbb{C}_{Ri}^\delta$.

The stability function 28 plays a similar role as the more elaborate stability functions used in two-equation models (Burchard & Bolding, 2001), which are derived from a second-moment closure. The stability functions in Equation 28 are plotted in the left panel of Figure 3 (see Section 4 for how the parameters are obtained via calibration to LES). Note that the form of the stability functions in 28 imply that Pr is constant in the limit $Ri \rightarrow 0$ and $Ri \rightarrow \infty$, which Venayagamoorthy and Stretch (2010) argue is inconsistent with direct numerical simulation (DNS) data. An extensive exploration of different formulations for \mathbb{S}_ψ is beyond the scope of the present work but remains an important direction for future research.

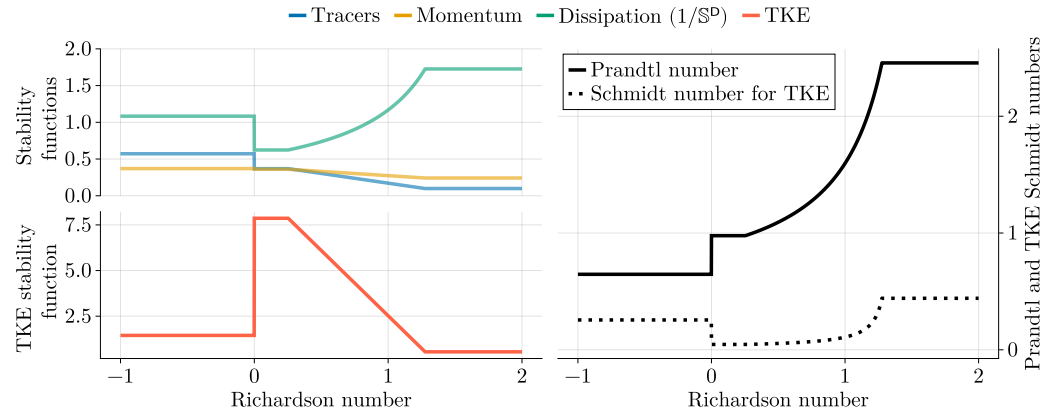


Figure 3. Stability functions (left panel), and Prandtl numbers and Schmidt numbers (right panel), computed with parameters calibrated against LESs as described in Section 4. The stability functions for tracers, momentum, and turbulent kinetic energy (TKE) are given by \mathbb{S}_ψ in 28. The stability function for dissipation length scale is $1/\mathbb{S}_D$. The Prandtl number is $\mathbb{S}_u/\mathbb{S}_e$ and the Schmidt number for TKE is $\mathbb{S}_u/\mathbb{S}_e$.

The four shear length scales introduce 15 free parameters: \mathbb{C}^s , \mathbb{C}_{Ri}^δ , and \mathbb{C}_{Ri}^0 used in all four length scales, along with 12 additional parameters associated with the coefficients \mathbb{C}_ψ^- , \mathbb{C}_ψ^0 , and \mathbb{C}_ψ^∞ for each length scale respectively.

3.1.2. Turbulent Prandtl and Schmidt Numbers in Stably Stratified Shear Turbulence

CATKE's Pr in 27 is a rational function of Ri , slightly different from the piecewise linear formulation proposed by Blanke and Delecluse (1993) and Madec et al. (2017). In particular,

$$Pr = \begin{cases} \mathbb{C}_u^-/\mathbb{C}_c^- & Ri < 0 \\ \mathbb{C}_u^0/\mathbb{C}_c^0 & 0 \leq Ri \leq \mathbb{C}_{Ri}^0 \\ \frac{\mathbb{C}_u^0 + \mu_u(Ri - \mathbb{C}_{Ri}^0)}{\mathbb{C}_c^0 + \mu_c(Ri - \mathbb{C}_{Ri}^0)} & \mathbb{C}_{Ri}^0 < Ri < \mathbb{C}_{Ri}^0 + \mathbb{C}_{Ri}^\delta \\ \mathbb{C}_u^\infty/\mathbb{C}_c^\infty & Ri \geq \mathbb{C}_{Ri}^0 + \mathbb{C}_{Ri}^\delta \end{cases}, \quad (29)$$

where $\mu_\psi \stackrel{\text{def}}{=} (\mathbb{C}_\psi^\infty - \mathbb{C}_\psi^0)/\mathbb{C}_{Ri}^\delta$. Similarly, the Schmidt number for TKE transport in stably-stratified shear turbulence is $Sc \stackrel{\text{def}}{=} K_u/K_e$. The Prandtl number and Schmidt number for calibrated parameters are visualized in the right panel Figure 3.

3.1.3. Neutral, Self-Similar, Wave-Modulated, Non-Rotating, Near-Surface Mixing

To interpret CATKE's mixing length near the surface in neutrally-stratified ($\partial_z b = 0$) conditions, when $\ell_\psi \sim d$, we consider quasi-equilibrium ($\partial_t u \approx \partial_t e \approx 0$), non-rotating ($f = 0$) near-surface turbulence driven by wind stress $\tau = \tau_x \hat{x}$. We suppose that the CATKE-parameterized single column Equations 13–15 and 19 possess a similarity solution in this scenario (Von Kármán, 1931),

$$\partial_z u \approx \frac{u_*}{\kappa d}, \quad (30)$$

where u_* is the friction velocity defined in Equation 21 (here simply $\sqrt{|\tau_x|}$), $d = -z$ is the distance to the surface, and κ is a constant parameter. If the ocean surface were rigid, κ could be interpreted as the von Kármán constant. But because the LES we use in this paper include surface wave effects, κ has a slightly different interpretation—as a “wave-modified” similarity layer constant, perhaps, as proposed by Samelson (2022).

To express κ in terms of CATKE's free parameters, we begin by assuming a balance between shear production and dissipation and neglecting diffusive turbulent transport to simplify 19 to

$$K_u(\partial_z u)^2 \approx \frac{e^{3/2}}{\ell_D}. \quad (31)$$

Note that in neutral conditions,

$$K_u = \mathbb{C}_u^0 \mathbb{C}^s d \sqrt{e}, \quad \text{and} \quad \ell_D = \frac{\mathbb{C}_D^s}{\mathbb{C}_D^0} d. \quad (32)$$

Inserting 30 and 32 into 31 and rearranging, we find an expression that relates the constant κ , u_\star , and e ,

$$\frac{u_\star^2}{e} \approx \kappa^2 \frac{\mathbb{C}_D^0}{\mathbb{C}_u^0 (\mathbb{C}^s)^2}. \quad (33)$$

Notice that e is independent of d in this expression. This means that neglecting turbulent transport in 31 in the context of the similarity hypothesis (30) is self-consistent. Next, integrating the quasi-equilibrium x -momentum equation $0 \approx \partial_z(K_u \partial_z u)$ from $z = 0$ to $z = -d$ yields

$$\partial_z u \approx \frac{u_\star}{d} \underbrace{\frac{u_\star}{\mathbb{C}_u^0 \mathbb{C}^s \sqrt{e}}}_{=1/\kappa}, \quad (34)$$

where we have used the neutral momentum diffusivity in 32 and the friction velocity definition $-K_u \partial_z u|_{z=0} = u_\star$. Equation 34 identifies κ by comparison to 30. We next use 33 to eliminate u_\star/\sqrt{e} and obtain an expression for CATKE's wave-modified similarity layer constant κ ,

$$\kappa \stackrel{\text{def}}{=} \mathbb{C}^s \left[(\mathbb{C}_u^0)^3 \mathbb{C}_D^0 \right]^{1/4}. \quad (35)$$

3.1.4. Steady-State Gradient Richardson Number for Stably Stratified Shear Turbulence

CATKE's dependence on the stable length scale $\ell \sim \sqrt{e}/N$ is associated with a steady-state gradient Richardson number in stably-stratified shear turbulence (Blanke & Delecluse, 1993). To see this, we first note that in stable stratification and far from boundaries, the mixing and dissipation length scales become

$$\ell_\psi = \mathbb{S}_\psi \frac{\sqrt{e}}{N} \quad \text{for} \quad \psi \in (u, c, e) \quad \text{and} \quad \ell_D = \frac{1}{\mathbb{S}_D} \frac{\sqrt{e}}{N}. \quad (36)$$

Inserting 36 into 19 and neglecting turbulent transport (equivalently, assuming spatially-uniform e) yields

$$\partial_t e = \underbrace{N(\mathbb{S}_c + \mathbb{S}_D)}_{\stackrel{\text{def}}{=} r} \left(\frac{Ri^\dagger}{Ri} - 1 \right) e, \quad (37)$$

where r is a rate, and

$$Ri^\dagger \stackrel{\text{def}}{=} \frac{\mathbb{S}_u}{\mathbb{S}_c + \mathbb{S}_D}. \quad (38)$$

when $Ri = Ri^\dagger$, the shear production of TKE is perfectly balanced by TKE destruction via buoyancy flux and dissipation, such that $r = 0$ and $\partial_t e = 0$. We therefore call Ri^\dagger the “steady-state Richardson number”. If

$Ri < Ri^\dagger$, then TKE and mixing will increase, while if $Ri > Ri^\dagger$ then TKE will decay and mixing will be suppressed. As a result—and as illustrated in Section 5.3 and Figure 12— Ri is driven toward Ri^\dagger in forced stratified shear turbulence. Finally we note that the functions \mathbb{S}_ψ , defined in 28, depend on Ri . For example, if $Ri < \mathbb{C}_{Ri}^0$, then $Ri^\dagger = \mathbb{C}_u^0/(\mathbb{C}_c^0 + \mathbb{C}_D^0)$. But if $Ri^\dagger > \mathbb{C}_{Ri}^0 + \mathbb{C}_{Ri}^\delta$, then $Ri^\dagger = \mathbb{C}_u^\infty/(\mathbb{C}_c^\infty + \mathbb{C}_D^\infty)$.

3.1.5. Convective Turbulence Length Scale

To formulate a length scale for free convection, we divide the freely convecting boundary layer into two regions: a “convecting layer” with unstable $N^2 < 0$, and a “penetration layer” with thickness δ . In the penetration layer, $N^2(z) > 0$ but $N^2(z + \delta) < 0$, where we note that the vertical coordinate z increases upwards and is defined such that $z < 0$. We use “penetration layer” rather than “entrainment layer” used by Deardorff (1970) to avoid confusion with lateral entrainment.) Our formulation for the convective length scale models both rapid mixing in the convective layer as well as entrainment into the boundary layer from below by plumes plunging through the convecting layer into the stably-stratified penetration layer below.

Our dynamic length scale for mixing in the convective layer is based on a dimensional analysis first proposed by Deardorff (1970) that links the turbulent velocity \sqrt{e} (m s^{-1}), surface buoyancy flux J_b (m^2/s^3), and convective layer depth, h (m),

$$\sqrt{e} \sim (h J_b)^{1/3}. \quad (39)$$

Recasting 39 in terms of a time-scale $t_{\text{mix}} \sim h/\sqrt{e}$ for convective mixing over the depth h yields

$$t_{\text{mix}} \sim \left(\frac{h^2}{J_b}\right)^{1/3}. \quad (40)$$

But if we represent convection as a diffusive process with diffusivity K_c , then we also have that

$$t_{\text{mix}} \sim \frac{h^2}{K_c}. \quad (41)$$

Equating 40 and 41 yields a scaling relation for the convective diffusivity K_c .

Now consider convection driven by constant destabilizing buoyancy fluxes J_b and increasing $h(t)$: according to (40), the mixing time then evolves according to $t_{\text{mix}} \sim h^{2/3}$. On the other hand, if we instead we impose a constant K_c —a commonly used parameterization when $N^2 < 0$ (Gutjahr et al., 2021; Jungclaus et al., 2022; Kuhlbrodt et al., 2018; Madec et al., 2017)—then 41 implies that, spuriously, $t_{\text{mix}} \sim h^2$. Thus, constant CA diffusivities inaccurately exhibit $t_{\text{mix}} \sim h^2$ and may produce bias when convection competes with other processes such as lateral restratification, or biogeochemical production and destruction.

To capture t_{mix} consistently between 40 and 41 over the convective region where $N^2 < 0$, we introduce a dynamic convective mixing length scale ℓ_ψ^h that scales with h ,

$$\ell_\psi^h \stackrel{\text{def}}{=} \mathbb{C}_\psi^h \frac{e^{3/2}}{\tilde{J}_b + J_b^{\min}} \sim h, \quad (42)$$

where J_b^{\min} is chosen small enough to have no impact on CATKE-parameterized solutions, and \tilde{J}_b is an estimate of the slowly-evolving part of the buoyancy flux J_b averaged over time-scales $t \sim t_{\text{mix}}$. We compute \tilde{J}_b by integrating

$$\partial_t \tilde{J}_b = \underbrace{\left(\frac{J_b}{\ell_D^2(z=0)}\right)^{1/3}}_{\sim t_{\text{mix}}^{-1}} (J_b - \tilde{J}_b), \quad (43)$$

where ℓ_D is the dissipation length scale and $(\ell_D^2/J_b)^{1/3} \sim t_{\text{mix}}$ scales with the instantaneous convective mixing time. Equation 43 relaxes \tilde{J}_b to J_b over t_{mix} . We use the dissipation length scale ℓ_D in 43 rather than a mixing length because we hypothesize that the convective turbulence evolution time-scale is most closely related to the time-scale for TKE dissipation rather than a mixing time-scale. In quasi-equilibrium, $\tilde{J}_b \approx J_b$. Because $\ell_\psi^h \sim h$, CATKE's convective tracer diffusivity scales with $K_c \sim h\sqrt{e}$.

The second objective of our convective mixing length formulation is to correctly predict the evolution of h . For this we introduce a model for “penetrative mixing” below the convective mixed layer associated with convective plumes that plunge through the mixed layer and penetrate into the strongly stratified region below. The “empirical law of convection” (Large et al., 1994; Siebesma et al., 2007; Souza et al., 2020, 2023; Van Roekel et al., 2018) is the observation, robust across a wide range of convective conditions, that penetrative fluxes at the penetration level z_p scale with

$$\overline{w'b'}|_{z=z_p} \sim -J_b \quad \text{such that} \quad h^2 \sim \frac{J_b t}{N^2}, \quad (44)$$

for initially-constant buoyancy gradient N^2 and constant buoyancy flux J_b .

To ensure that CATKE reproduces 44, we introduce a “penetrative mixing length”,

$$\ell_\psi^p \stackrel{\text{def}}{=} \mathbb{C}_c^p \frac{\tilde{J}_b}{N^2 \sqrt{e} + J_b^{\min}}, \quad (45)$$

which is applied within the aforementioned penetration layer at the depth z_p , defined via

$$N^2(z_p) > 0 \quad \text{and} \quad N^2(z_p + \delta) < 0, \quad (46)$$

where δ is the thickness of the penetration layer. At $z = z_p$, 45 produces $\overline{w'b'} = -\ell_c^p \sqrt{e} N^2 \approx -\mathbb{C}_c^p J_b$ in accordance with the empirical law in 44. Our numerical implementation of the convective mixing length uses $\delta = \Delta z$ where Δz is the grid spacing at z_p . This assumes that the entrainment layer is thinner than the grid spacing: when $\delta > \Delta z$, CATKE solutions may exhibit a “thin entrainment layer bias” even if the boundary layer deepening rate is correct.

The scaling $h \sim e^{3/2}/J_b$ is an overestimate when e is produced by both shear and convective buoyancy flux. Since the total mixing length ℓ_ψ takes the maximum between the convective and shear mixing lengths, blending the length scales in a mixed turbulence regime requires a way to reduce the convective mixing length in the presence of significant shear production. For this purpose we introduce an estimate of the flux Richardson number in near-neutral conditions,

$$\widetilde{Ri_f} \stackrel{\text{def}}{=} \frac{d\sqrt{e}|\partial_z \mathbf{u}|^2}{\tilde{J}_b + J_b^{\min}}, \quad (47)$$

where $d = -z$ is depth. $\widetilde{Ri_f}$ in 47 measures the relative contribution of shear production (the numerator) versus buoyancy flux (the denominator) to the TKE budget in unstable stratification. We then use this estimate to reduce the convective mixing length by

$$e_{sp} \stackrel{\text{def}}{=} \max\left(0, 1 - \mathbb{C}^{sp} \widetilde{Ri_f}\right), \quad (48)$$

where \mathbb{C}^{sp} is a free parameter. The reduction factor 48 may also be interpreted as modeling how shear disrupts coherent plumes and thereby reduces convective turbulence correlation scales. Note that the numerator in 47 estimates shear production using the mixing length d , which is appropriate for shear-driven turbulent mixing. This formulation means that the free convection length scale is more limited at depth, where convective plumes are less connected to destabilizing surface buoyancy fluxes.

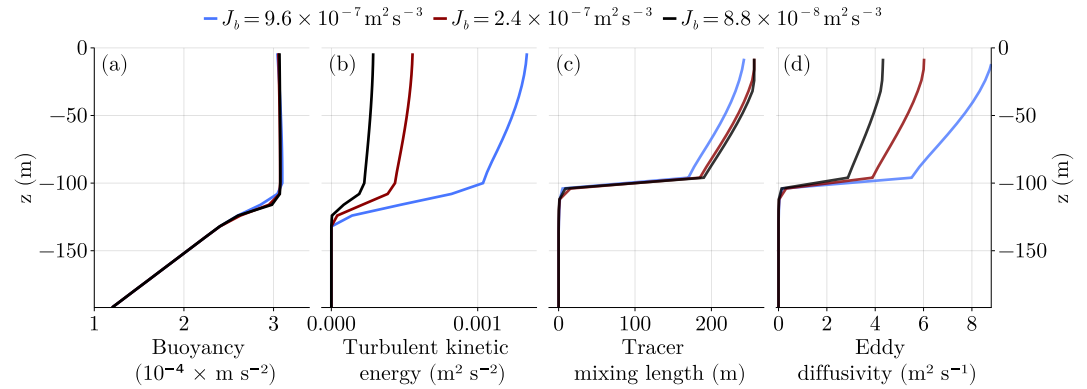


Figure 4. CATKE mixing length and eddy diffusivity during free convection for three cases with boundary layer depth $h \approx 100$ m. (a) CATKE-predicted buoyancy profiles for the three cases, (b) profiles turbulent kinetic energy TKE, e , (c) tracer mixing lengths ℓ_c , (d) tracer eddy diffusivities K_c . The buoyancy fluxes J_b correspond to heat fluxes $Q \approx 2000, 500$, and 183 W m^{-2} using $Q \approx \rho_o c_p J_b / \alpha g$ and $\rho_o = 1024 \text{ kg m}^{-3}$, $c_p = 3991 \text{ J } ^\circ\text{C}^{-1}$, $\alpha = 2 \times 10^{-4} \text{ } ^\circ\text{C}^{-1}$, and $g = 9.81 \text{ m s}^{-2}$.

Putting 42, 45, and 48 together yields the piecewise parameterization

$$\ell_\psi^{\text{conv}}(z) = \epsilon_{sp} \begin{cases} \ell_\psi^h & \text{if } N^2 < 0 \text{ and } J_b > 0, \\ \ell_\psi^p & \text{if } N^2 > 0, N^2(z + \Delta z) < 0, \text{ and } J_b > 0, \\ 0 & \text{otherwise.} \end{cases} \quad (49)$$

figure 4 illustrates the behavior of the convective length scale predicted by CATKE in 49 for three free convection cases with surface buoyancy fluxes $J_b = 9.6 \times 10^{-7}, 2.4 \times 10^{-7}$, and $8.8 \times 10^{-8} \text{ m}^2 \text{ s}^{-3}$ integrated for 6, 24, and 72 hr respectively, using the initial buoyancy profile in Equation A1, which is also used for all our LES. The parameters used to make Figure 4 are automatically calibrated to LESs, as described in Section 4. Figure 4a shows CATKE-simulated buoyancy profiles after integrating for 6, 24, and 72 hr Figure 4b shows that stronger forcing cases have greater levels of TKE. Figure 4c shows the tracer mixing length, which above $z = -100$ meters is dominated by the convective mixing length. Though each case has different TKE and different surface buoyancy flux, they nevertheless predict similar tracer mixing lengths, corroborating the dimensional analysis in Equation 39. (We also note that the mixing lengths are twice the boundary layer depth. We discuss this and other possible biases in free convection further in Section 4.) Figure 4d shows the eddy diffusivity for the three cases—unlike a typical constant-diffusivity CA model, CATKE’s “convective adjustment diffusivity” varies depending on the strength of the surface buoyancy flux. Because the predicted mixing length is similar for all three cases, the tracer diffusivity varies with the surface buoyancy flux due to variation in the TKE.

4. A Posteriori Calibration Against Large Eddy Simulations

We calibrate CATKE’s 23 free parameters in an a posteriori (Duraiamy, 2021; Frezat et al., 2022) single-column context using horizontally-averaged data from 21 LES described in Section 2 and Appendix A. A posteriori calibration estimates free parameters by minimizing the error between LES data— $b(z, t)$, $u(z, t)$, $v(z, t)$, and the forced passive tracer $c(z, t)$ extracted from solutions of 1–3—and single column simulations of b , u , v , and c in 13–15 that use CATKE as a parameterization. The minimization is computed over the whole time series and thus in a posteriori calibration free parameters are determined by directly minimizing simulation bias. In this way, a posteriori calibration incorporates numerical and other errors that accumulate during a simulation. Moreover, a posteriori calibration can leverage any observational data computable from the predicted solution, even only indirectly informative data. For example, in this work we calibrate elements of the TKE equation using only horizontally-averaged momentum and buoyancy profiles derived from LES.

4.1. The Importance of a Posteriori Calibration

Explicitly minimizing simulation bias distinguishes a posteriori calibration from other methods that minimize other biases that are only indirectly related to simulation bias—for example, by attempting to compute free parameters directly from data, usually by considering subcomponents of the parameterization in isolation (examples may be found in Umlauf & Burchard, 2003; Reichl & Li, 2019). These latter methods are called “a priori” (Duraismy, 2021), because they hinge on additional (often problematic) hypotheses—such as an assumption of structurally perfect, unbiased parameterization (permitting a direct computation of free parameters from limited data), or an assumption that free parameters are uncorrelated with one another (permitting free parameters to be determined in isolated contexts, rather than leveraging all data simultaneously).

To illustrate the pitfalls of a priori calibration, we consider integrating a CATKE-parameterized single column equation for buoyancy b ,

$$\partial_t b = -\underbrace{\partial_z \mathcal{J}(b; \mathbb{C})}_{\text{CATKE}} + \underbrace{\xi}_{\text{noisy error}}. \quad (50)$$

In 50, we include two terms: (a) the divergence of a parameterized flux \mathcal{J} that depends on both the simulated buoyancy b (omitting here for simplicity other aspects of the state such as u or v) and a set of free parameters \mathbb{C} , and (b) an explicit “error” term ξ that represents spatial and temporal discretization errors. We additionally define the ideal or “perfect” solution as \hat{b} . When Equation 50 is integrated forward to predict the evolution of b , fluctuations away from the perfect solution \hat{b} inevitably develop due both to structural errors in \mathcal{J} and because of the discretization error ξ , leading to an error $= b - \hat{b}$ that grows as \sqrt{t} (see, for example Gardiner, 2021).

This error accumulation is potentially fatal for *a-priori*-calibrated parameterizations: because the parameters \mathbb{C} are determined by evaluating $\mathcal{J}(\hat{b})$ in terms of the *perfect* \hat{b} , while the predictions $\mathcal{J}(b)$ made in terms of the noisy b are unconstrained by the calibration procedure. At best, the unconstrained predictions $\mathcal{J}(b)$ are inaccurate. At worst, however, the errors $\mathcal{J}(b) - \mathcal{J}(\hat{b})$ self-amplify without bound, thwarting prediction altogether (Brenowitz & Bretherton, 2019; Rasp, 2020; Rasp et al., 2018).

A posteriori calibration avoids all of these pitfalls by definition, since $\mathcal{J}(b, \mathbb{C}_*)$ computed in terms of the simulated b and optimal parameters \mathbb{C}_* is explicitly constrained by minimizing the discrepancy between $\mathcal{J}(b, \mathbb{C})$ and data. Put differently: a posteriori calibration “teaches” \mathcal{J} how to make accurate, stable predictions in terms of potentially noisy inputs b . We leverage this feature to realize a key innovation of this work: we explicitly minimize spatial discretization error by including single-column simulations with 2-, 4-, and 8-m resolution in our loss function.

4.2. Ensemble Kalman Inversion for a Posteriori Calibration

To solve the nonlinear inverse problem posed by a posteriori calibration, we use an ensemble-based method called Ensemble Kalman Inversion (EKI; Iglesias et al., 2013). An advantage of EKI is that it is gradient-free, requiring only the ability to run an ensemble of simulations with different parameters. The EKI algorithm can be construed either as the integration of a dynamical system or as an iterative scheme for repeatedly refining an initial distribution of free parameter values.

EKI minimizes the objective function

$$\Phi(\mathcal{G}, \mathcal{Y}; \mathbb{C}) \stackrel{\text{def}}{=} \left\| \mathcal{M}^{-1/2} [\mathcal{G}(\mathbb{C}) - \mathcal{Y}] \right\|^2, \quad (51)$$

where \mathcal{Y} denotes a vector of observational data, $\mathcal{G}(\mathbb{C})$ denotes a parameterized prediction of the observations made with a set of free parameters \mathbb{C} , and \mathcal{M} is a matrix that represents the uncertainty of \mathcal{Y} . Φ measures the discrepancy between $\mathcal{G}(\mathbb{C})$ and \mathcal{Y} given uncertainty \mathcal{M} . The data \mathcal{Y} is extracted from 21 of the LES described in Table 1 that have intermediate surface forcing, each coarse-grained three times to 2-, 4-, and 8-m vertical resolution, respectively. \mathcal{G} is constructed by assembling $21 \times 3 = 63$ single column simulations, representing a prediction of each of the 21 LES cases at the three vertical resolutions.

We note that the near-surface dynamics in the LES seem uncertain. For example, the LES profiles exhibit strong unstable near-surface buoyancy gradients for strongly-forced convective cases, indicating that turbulent mixing is suppressed near the top of the LES domain. These features are robust to changes in LES resolution (see Appendix A) and may represent real physics, since the scale of turbulent motions is restricted by proximity to the ocean surface. However, it is also plausible that the LES are missing important mixing processes near a wavy, bubbly, broken ocean surface, such as wave breaking, or unresolved surface-wave-turbulence interactions. We therefore omit the top 4 m of the LES domain from the data vector \mathcal{Y} , and thereby avoid overconstraining parameters with the most uncertain elements of the LES data.

EKI finds a set of optimal parameters $\mathbb{C} = \mathbb{C}_*$ that minimize $\Phi(\mathcal{G}, \mathcal{Y}, \mathbb{C})$ in 51 by evolving an ensemble of parameter sets using the algorithm described in Appendix C. In this work we use relatively large ensembles with 1,000 members. This means that every EKI iteration requires $21 \times 3 \times 1000 = 63,000$ single column simulations, for 21 LES cases and 3 vertical resolutions. To make the calibration as efficient as possible, we implement CATKE in Oceananigans and leverage a feature that permits us to integrate an ensemble of single column models in parallel in the configuration of a single three-dimensional simulation on a GPU. As a result, each EKI iteration requires evolving 9 effectively three-dimensional simulations (3 resolutions for each of the 12-, 24- and 48-hr suites). On an Nvidia Titan V GPU and with 1,000 ensemble members, a single EKI iteration takes 40–50 s, and the entire calibration takes 4–6 hr. In the course of this work we have performed complete calibrations of CATKE's parameters hundreds of times—to experiment with new formulations, new numerical schemes, and to tweak the calibration setup. This workflow represents a new “calibration-based” paradigm in parameterization development, where physical formulation or numerical implementation changes are tested against the baseline by comparing predictions for independently calibrated parameterizations. The 23 calibrated free parameters that correspond to the version of CATKE described in this paper and the previously described LES are listed in Table 3.

5. Validation

We next assess CATKE's ability to make accurate predictions in a single column context with the free parameters listed in Table 3. First, we derive quantities with well-understood physical interpretations from CATKE's free parameters, and evaluate whether their calibrated values are close to values reported in the literature. Second, we compare CATKE-parameterized simulations both to the 21 constant-forcing LES used for calibration and to an additional 12 constant-forcing LES that are both more strongly and more weakly forced than the calibration LES. Third, we conduct a 34-day CATKE-parameterized simulation of equatorial deep-cycle turbulence using the data set provided by Whitt et al. (2022), and then compare the results to the LES used therein. This third validation context is useful because it involves both time-dependent surface forcing, solar insolation, and lateral flux divergences derived from a high resolution tropical general circulation model (GCM). Finally, we evaluate CATKE's sensitivity to vertical resolution and time-step size. These all provide a measure of confidence in CATKE's ability to not only represent the LES data used for calibration but also to extrapolate to differently-forced conditions, time-dependent surface forcing, and GCM-like contexts that include interactions with other parameterizations and lateral flux divergences from for example, the advection of momentum, temperature, and salinity. All of this said, we maintain a caveat that CATKE should still be assessed, and likely recalibrated, in a regional or global context involving lateral fluxes and interactions with other model components.

5.1. Derived Quantities

Table 4 shows several quantities that can be derived or computed in terms of CATKE's calibrated free parameters. There is unknown uncertainty in these estimates, so the precise values must be taken with a grain of salt. Uncertainty quantification, using the methodology proposed by Cleary et al. (2021) for example, is left for future work.

5.1.1. Steady-State Richardson Number

Section 3.1.4 shows how a steady-state Ri may be derived from CATKE's TKE equation. From the parameters in Table 3, we find that

Table 3
A Summary of CATKE's Free Parameters

Symbol	Description	Optimal value	Bounds
C_J^{shear}	Wind stress TKE surface flux	3.18	(0, 8)
C_J^{conv}	Convective TKE surface flux	0.38	(0, 8)
C^s	Near-surface mixing scale	1.13	(0, 2)
C_c^h	Tracer free convection scale	4.79	(0, 8)
C_c^-	Tracer mixing for negative Ri	0.57	(0, 2)
C_c^0	Tracer mixing for near-neutral Ri	0.37	(0, 2)
C_c^∞	Tracer mixing for high Ri	0.098	(0, 2)
C_c^p	Tracer free entrainment scale	0.11	(0, 2)
C_u^h	Momentum free convection scale	3.71	(0, 8)
C_u^-	Velocity mixing for negative Ri	0.37	(0, 2)
C_u^0	Velocity mixing for near-neutral Ri	0.36	(0, 2)
C_u^∞	Velocity mixing for high Ri	0.24	(0, 2)
C_e^h	TKE free convection scale	3.64	(0, 10)
C_e^-	TKE transport for negative Ri	1.44	(0, 10)
C_e^0	TKE transport for near-neutral Ri	7.86	(0, 10)
C_e^∞	TKE transport for high Ri	0.55	(0, 10)
C_D^h	Dissipation free convection scale	3.25	(0, 10)
C_D^-	Dissipation scale for negative Ri	0.92	(0, 10)
C_D^0	Dissipation scale for near-neutral Ri	1.60	(0, 10)
C_D^∞	Dissipation scale for high Ri	0.58	(0, 10)
C_{Ri}^0	Stability function transitional Ri	0.25	(0, 2)
C_{Ri}^δ	Stability function Ri width	1.02	(0, 2)
C^{sp}	Sheared plume scale	0.50	(0, 2)

Note. Note that “near-neutral Ri ” means $Ri \leq C_{Ri}^0$, while “high Ri ” means $Ri \geq C_{Ri}^0 + C_{Ri}^\delta$. The bounds limit the values a parameter can take during calibration, using the method described in C3. The prior distributions for each parameter span the range between the bounds.

$$Ri^\dagger \stackrel{\text{def}}{=} \frac{C_u^0}{C_c^0 + C_D^0} \approx 0.18, \quad (52)$$

which lies in the “near-neutral” stability function regime, since $C_{Ri}^0 = 0.25 > Ri^\dagger$. $Ri^\dagger = 0.18$ is somewhat less than the 0.23 used by Blanke and Delecluse (1993), or the value $Ri = 1/4$ that determines the stability of a laminar stratified shear layer. In Section 5.3, we find that Ri^\dagger is a crucial parameter controlling mixing in forced stably-stratified turbulence, and that LES tend to exhibit Ri in the range 0.2–0.23.

5.1.2. Near-Surface Similarity Constant

Section 3.1.3 shows how a near-surface similarity constant—analogue to the von Kármán constant for turbulence near rigid non-wavy walls—may be computed from the near-wall and momentum stability function parameters. From Table 3 and Equation 35 we find that

$$\kappa = C^s \left[(C_u^0)^3 C_D^0 \right]^{1/4} \approx 0.47, \quad (53)$$

which is slightly higher than the rigid-wall von Kármán constant value of 0.4. A slightly higher similarity constant is consistent with the notion that surface waves act to increase the coherence of turbulent motions, which increases mixing lengths and suppresses TKE dissipation.

A similar wave-induced enhancement to the similarity constant is proposed by Samelson (2022). However, Samelson (2022) models the enhancement as a function of wind at 10 m height, u_{10} . In our case, the LES are forced with varying u_{10} , but constant Langmuir number $La \approx 0.3$ (see Table 1 for a summary of the LES cases). Thus we must either hypothesize that surface waves can be modeled with a La -dependent enhancement of κ , or that CATKE is missing physics. We are unable to proceed further in determining wave-induced enhancements to κ without LES that vary La , so we save such considerations for future work.

Table 4
A Summary of Parameters and Non-Dimensional Numbers Derived From CATKE's Calibrated Free Parameters

Symbol	Value	Description
Ri^\dagger	0.18	Steady-state gradient Richardson number
κ	0.47	Near-neutral near-surface similarity constant
Pr_0	0.98	Near-neutral turbulent Prandtl number ($Ri \rightarrow 0$)
Pr_∞	2.46	Strongly-stratified turbulent Prandtl number ($Ri \rightarrow \infty$)
Pr_-	0.65	Unstably-stratified shear turbulence Prandtl number ($Ri < 0$)
Pr_c	0.77	Free convection turbulent Prandtl number ($Ri \rightarrow -\infty$)
Γ_0	0.23	Near-neutral mixing coefficient ($Ri \rightarrow 0$)
Γ_∞	0.17	Strongly-stratified mixing coefficient ($Ri \rightarrow \infty$)
Sc_0	0.046	Near-neutral turbulent TKE Schmidt number ($Ri \rightarrow 0$)
Sc_∞	0.44	Strongly-stratified turbulent TKE Schmidt number ($Ri \rightarrow \infty$)
Sc_-	0.26	Unstably-stratified shear turbulence TKE Schmidt number ($Ri < 0$)
Sc_c	1.02	Free convection turbulent TKE Schmidt number ($Ri \rightarrow -\infty$)

5.1.3. The Turbulent Prandtl Number

The turbulent Prandtl number is defined as

$$Pr \stackrel{\text{def}}{=} \frac{K_u}{K_c}, \quad (54)$$

which is derived for CATKE in Section 3.1.1. For various regimes of turbulence we obtain.

- $Pr_c \approx 0.77$ for weakly-sheared convection,
- $Pr_- \approx 0.65$ for unstably-stratified shear turbulence,
- $Pr_0 \approx 0.98$ for near-neutral shear turbulence,
- $Pr_\infty \approx 2.46$ for strongly-stratified shear turbulence.

A turbulent Pr that increases from less than unity to above unity as Ri crosses zero is consistent with laboratory and DNS studies (e.g., D. Li, 2019), as well as typical two-equation models (e.g., Burchard & Bolding, 2001). On the other hand, one-equation models (Blanke & Delecluse, 1993; Madec et al., 2017) often prescribe Pr to a value of 10 or higher as Ri tends to infinity. It is unlikely that our boundary layer LES are informative for such high Ri mixing, so more LES are needed to assess and perhaps refine CATKE's stability function to capture very high Ri regimes.

5.1.4. The Turbulent Schmidt Number

Calibration determines that $Sc = 0.26$ for unstably-stratified shear turbulence with $Ri < 0$, and then varies between $0.046 < Sc < 0.44$ as Ri increases from 0 to $\mathbb{C}_{Ri}^0 + \mathbb{C}_{Ri}^\delta$. As a result, TKE is transported much more rapidly than momentum or tracers in shear-dominated turbulence, and similarly to momentum or tracers in convective or weakly-sheared stratified turbulence. Rapid TKE diffusion relative to momentum or tracer diffusion introduces an “implicitly non-local” element to CATKE's mixing predictions, because TKE transport can generate mixing in a region that is displaced from the region of TKE generation.

5.1.5. Stratified Turbulence Mixing Coefficient

The “mixing coefficient”—the ratio between buoyancy flux and dissipation in stably-stratified turbulence (Gregg et al., 2018; C.-c. P. Caulfield, 2020)—measures the relative level of TKE converted to potential energy in the process of mixing buoyancy versus TKE dissipation. Using 19 and assuming stably-stratified turbulence far from boundaries such that $\ell_c = \mathbb{S}_c \sqrt{e}/N$, $\ell_D = \sqrt{e}/(\mathbb{S}_D N)$, and $K_c = \mathbb{S}_c e/N$, we find that

$$\Gamma \stackrel{\text{def}}{=} \frac{\text{buoyancy flux}}{\text{dissipation}} = \frac{\mathbb{S}_c}{\mathbb{S}_D}. \quad (55)$$

The free parameters in Table 3 imply that the mixing coefficient Γ varies between $\Gamma_0 \approx 0.26$ for near-neutral turbulence and $\Gamma_\infty \approx 0.17$ for strongly-stratified (shear-free) turbulence. The latter is applicable to internal wave breaking, where an extensive literature suggests that $\Gamma_\infty \approx 0.2$ (Gregg et al., 2018).

5.2. Validation Against Constant-Forcing LES and Comparison With Other Parameterizations

In this section, we validate CATKE's ability to make predictions both within and outside the range of surface forcings used for calibration. To add context to this validation exercise and connect with other studies, we include a comparison with predictions from the K -profile parameterization (KPP; Large et al., 1994), and the “Langmuir turbulence” second-moment closure (SMC-LT) described by Harcourt (2015), whose results depend additionally on the Stokes drift profile we used for LES. All simulations, including those with KPP and SMC-LT, use staggered vertical grids with 128 cells, in a 256-m deep domain with 2-m vertical resolution. We use a 2-min time step for CATKE and KPP, and a 1-s time-step for SMC-LT. Such a short time-step was used for SMC-LT because we observed that the results were sensitive to time steps 20 s and longer for the strong forcing cases.

We should treat these comparisons with some caution: KPP or SMC-LT were calibrated to different data sets than what we use for CATKE. Moreover, uncertainty in the accuracy of LES profiles near the surface—where CATKE, KPP, and SMC-LT often exhibit significant discrepancies—prevent firm conclusions about near-

surface biases. That said, we find by manual inspection that for every constant-forcing case, CATKE predicts boundary layer depth simulated by LES—both inside and outside the training data set—more accurately than either KPP or SMC-LT. This is an important result because boundary layer depth is a key metric determining the short-term sensitivity of climate predictions (Gregory, 2000; Held et al., 2010). With this broad summary of CATKE's main successes stated, we focus the subsequent discussion for each case on CATKE's biases and areas to focus on for future improvements.

5.2.1. Constant Forcing Validation: Free Convection

We begin with the free convection cases plotted in Figure 5. The free convection cases represent some of the best predictions of KPP and SMC-LT. Boundary layer depth is well-predicted by all parameterizations to within 10 m, with perhaps the greatest bias coming from SMC-LT in the weakly-forced 72-hr case—despite that KPP has known structural biases for representing free convection (Souza et al., 2020). A large portion of the KPP profiles are stably-stratified within the boundary layer in our most strongly-forced convective cases. This bias, which is a known issue with KPP (see Section 8.6.3 in Griffies et al., 2015), is particularly prominent in the cases we consider due to the strength of our forcing and the weakness of our underlying stratification. Of the three, CATKE exhibits the most well-mixed boundary layers under very strong forcing due to its convective mixing length.

For near-surface buoyancy (and equivalently SST, or SST) the three parameterizations make different predictions. For example, CATKE predicts a warmer SST because of its near-neutral boundary layer profile. On the other hand KPP, SMC-LT, and the LES all exhibit layers of unstable stratification next to the surface, and thereby also predict substantially colder SST than CATKE. Such upper boundary layer structure sensitively depends on a description of how mixing is suppressed (or not) close to the ocean surface. Unfortunately, we are unsure how far to trust the LES results, which may be missing important processes associated with wave breaking or unresolved wave-turbulence interactions. Addressing near-surface uncertainties in the LES data, and thereby coming to stronger conclusions about the relative fidelity of CATKE, KPP, and SMC-LT, requires observations of near-surface boundary layer structure to either validate or motivate improvements to the LES. We leave this for future work.

The buoyancy profiles in Figure 5 reveal bias in CATKE's predictions of the detailed structure of the lower half of the convecting boundary layer. One contribution to this bias is well-known: in free convection, buoyancy fluxes in the lower half of the boundary layer are upgradient. In order to accurately capture the boundary layer depth, CATKE must accurately predict the buoyancy flux—and therefore cannot avoid erroneously predicting a slightly unstably stratified buoyancy profile where in the LES the profile is either nearly mixed or actually slightly stably stratified. No amount of calibration or additional free parameters can fix this bias given CATKE's downgradient formulation. The only solution is to introduce a non-downgradient, non-local contribution to CATKE's fluxes. For example, CATKE could be augmented with a mass flux scheme in the manner of Siebesma et al. (2007); Giordani et al. (2020). Other alternatives include evolving fluxes directly as in Garanaik et al. (2024), or adding prognostic tracer variances (Legay et al., 2024).

To investigate CATKE's free convection bias further, Figure 5 compares CATKE's predictions of the forced passive tracer profile with LES. This comparison reveals that while CATKE generally models the tracer profile well (except for the extreme, extrapolating, 6-hr case in panel a), CATKE tends to overmix especially in the lower part of the boundary layer, where the LES tracer profiles exhibit a slight peak and stronger gradients. Thus in addition to lacking a non-local contribution to fluxes, CATKE also overpredicts mixing to some degree, especially near the base of the boundary layer. The overprediction of mixing may be related to an overprediction of the tracer mixing length exhibited by Figure 4. Addressing this bias could motivate adding non-local contributions to convective fluxes as well as modifying the depth structure of the convective mixing length.

5.2.2. Constant Forcing Validation: Shear-Driven Turbulence

We next turn to pure shear- or wind-driven turbulence. We have two such cases, one without rotation and thus representing near-equatorial mixing, and a second with a Coriolis parameter of $f = 10^{-4} \text{ s}^{-1}$ corresponding to a latitude of about 43°N . The wind forcing that would produce the momentum flux applied to the strong wind, no rotation cases spans from 9 to 22 m s^{-1} . The wind forcing in the strong wind (and rotating) cases spans $15\text{--}24 \text{ m s}^{-1}$.

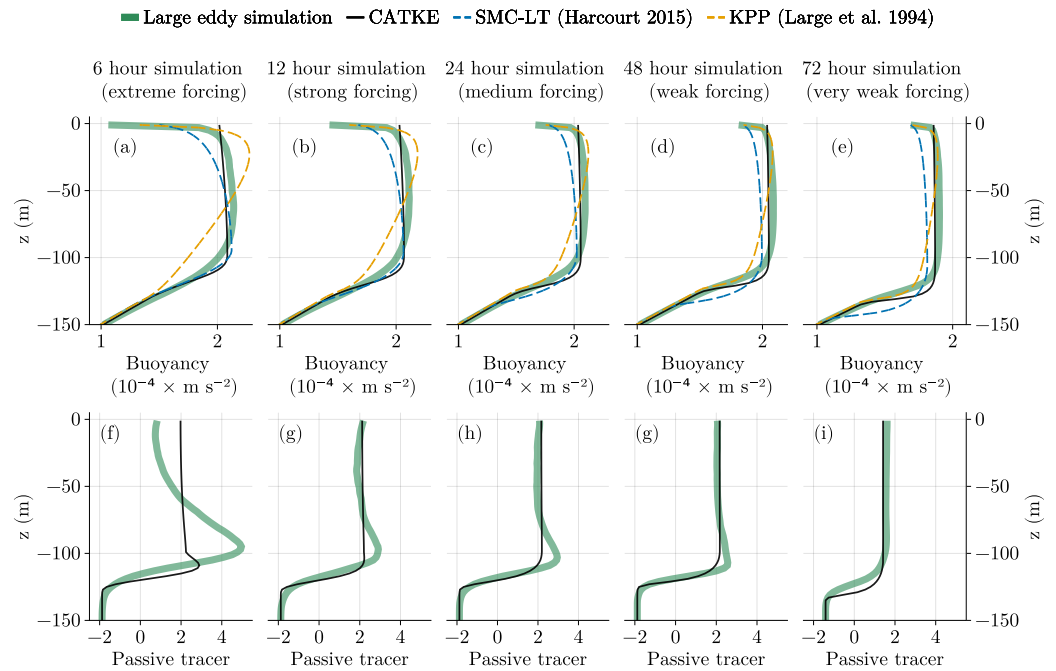


Figure 5. A four-way comparison for the “free convection” constant forcing cases described in 1 and Appendix A between horizontally-averaged LES, CATKE, the K -profile parameterization (KPP Large et al., 1994), and the Langmuir turbulence second moment closure (SMC-LT) described by Harcourt (2015) (SMC-LT). Both KPP and SMC-LT are implemented in the General Ocean Turbulence Model (GOTM, Burchard et al., 2006; Q. Li et al., 2019, 2021). Panels (a)–(e) compare buoyancy profiles in free convection with forcing of decreasing strength corresponding to the 6-, 12-, 24-, 48-, and 72-hr suites, respectively. The free convection cases have no wind forcing and destabilizing buoyancy fluxes that correspond, roughly, to heat fluxes between 181 and 2000 W m^{-2} . The initial condition is density stratified with a depth-varying buoyancy gradient that varies between 10^{-6} s^{-2} and $2 \times 10^{-5} \text{ s}^{-2}$. Panels (f)–(i) compare the profiles of a forced passive tracer simulated by LES with that simulated by CATKE. The passive tracer forcing, which is described in Appendix A2, is a Gaussian centered on $z = -96 \text{ m}$ and 8 m wide. The strength of the forcing depends on the suite: the 6-, 12-, 24-, 48-, and 72-hr suites use 15 min, 30 min, 1 hr, 2 hr, and 4 hr forcing time scales, respectively.

A comparison between LES, SMC-LT, KPP, and CATKE for the strong wind, no rotation case is shown in Figure 6. All parameterizations make similar and good predictions for boundary layer depth and surface temperature, except for SMC-LT in the 6-hr case, where it overmixes slightly. A comparison between CATKE and LES simulations of the forced passive tracer for the strong wind, no rotation case is shown in Figure 6, revealing that CATKE fares far better for this case than for free convection, and more specifically exhibits a slight tendency to overmix near the base of the boundary layer and to undermix near the surface.

The strong wind case with rotation plotted in Figure 7 proves more challenging for CATKE and extremely challenging for SMC-LT and KPP. For all forcing strength, SMC-LT and KPP exhibit serious shallow bias and warm SST bias. CATKE simulations, on the other hand, are better but still exhibit a tendency to overmix slightly, resulting in boundary layers that are approximately 5% too deep. Figure 7 compares CATKE and LES predictions of the forced passive tracer for the strong wind case, corroborating the “overmixing bias” especially for the 6- and 48-hr suites, while additionally revealing undermixing near the surface.

5.2.3. Constant Forcing Validation: Mixed Shear and Convective Turbulence

CATKE simulations are also more accurate than KPP or SMC-LT for cases involving both wind and destabilizing buoyancy forcing, which produces a mixed regime of turbulence with both shear and buoyant production of TKE. We have three mixed cases comprising a total of 15 LES with both wind and buoyancy forcing: strong wind, weak cooling, medium wind, weak cooling, and weak wind, strong cooling. Results for these 15 cases are shown in Figures 8–10. KPP exhibits significant shallow bias for all cases. SMC-LT exhibits less shallow bias than KPP, but still more than CATKE. CATKE’s worst performance is in the weak wind, strong cooling cases where it overmixes.

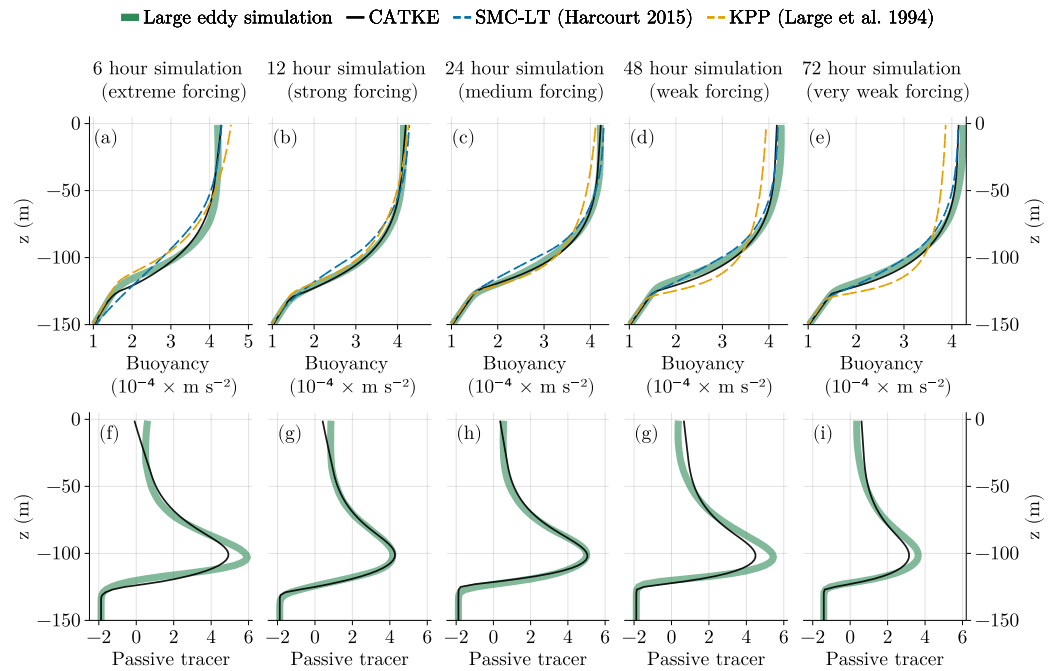


Figure 6. A comparison between LES and three turbulence closures (CATKE, KPP, and SMC-LT) for the “strong wind, no rotation” constant forcing cases described in Table 1 and Appendix A. Surface stresses correspond to $9\text{--}22\text{ m s}^{-1}$ 10-m winds. See Figure 5.

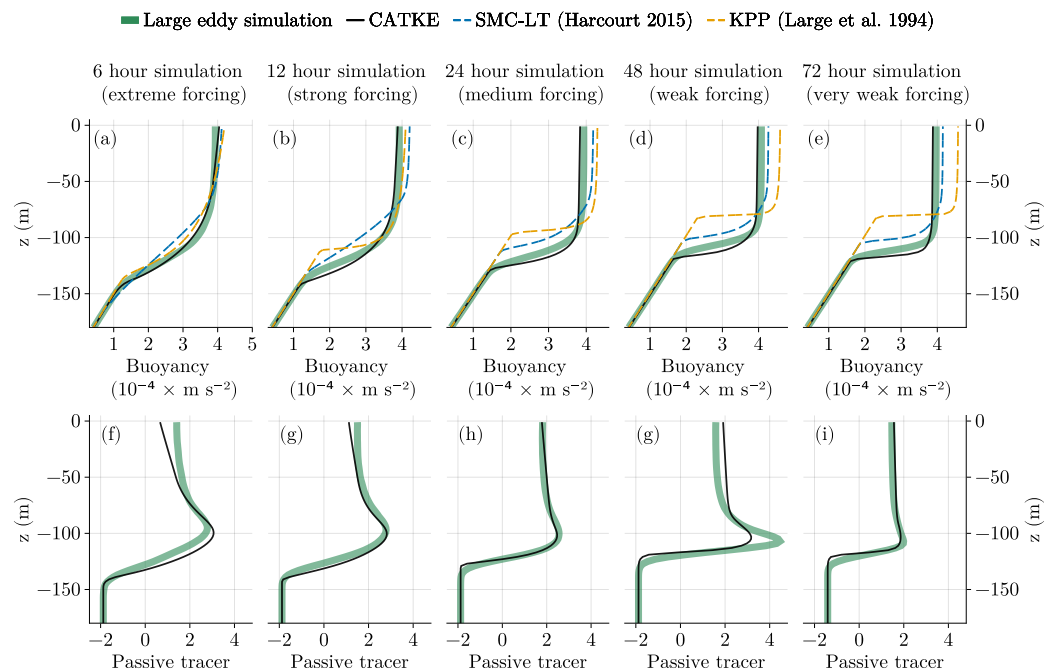


Figure 7. A four-way comparison between LES and three turbulence closures (CATKE, KPP, and SMC-LT) for the “strong wind” constant forcing cases described in Table 1 and Appendix A. The Coriolis parameter is $f = 10^{-4}\text{ s}^{-1}$ and surface stresses correspond to $15\text{--}24\text{ m s}^{-1}$ 10-m winds. See Figure 5.

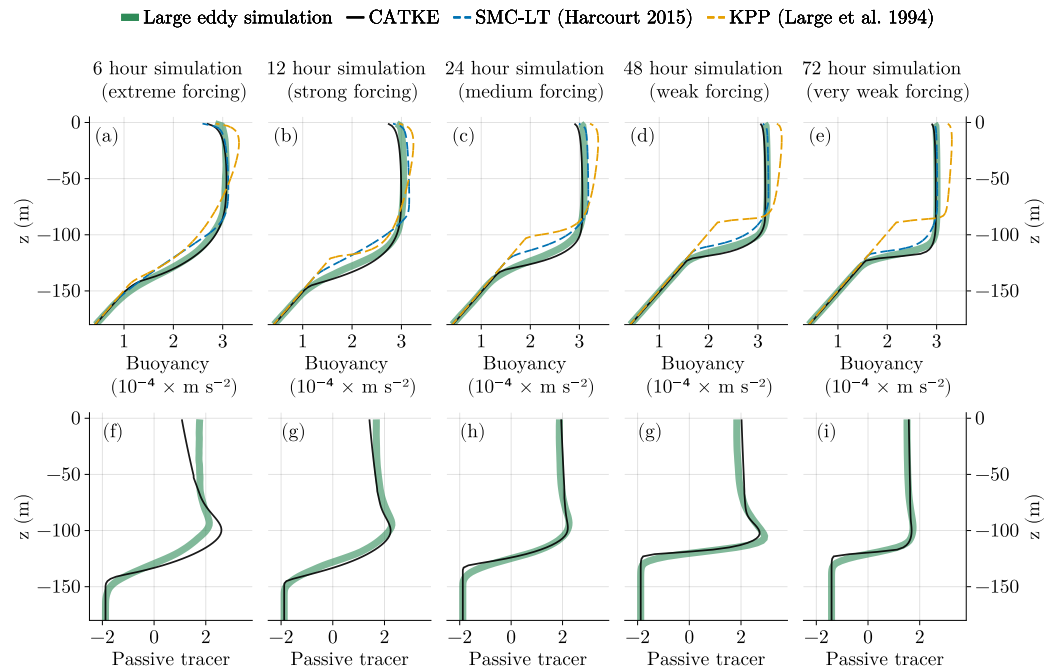


Figure 8. A four-way comparison between LES and three turbulence closures (CATKE, KPP, and SMC-LT) for the “strong wind, weak cooling” constant forcing cases described in Table 1 and Appendix A. The Coriolis parameter is $f = 10^{-4} \text{ s}^{-1}$, surface stresses correspond to 14–23 m s^{-1} 10-m winds, and surface cooling ranges from 79 to 833 W m^{-2} . See Figure 5.

Figures 8–10 also compare CATKE and LES predictions of the forced passive tracer for strong wind, weak cooling, mid wind mid cooling, and weak wind weak cooling cases. The most bias is exhibited in the weak wind strong cooling case, where it tends to overmix as exhibits in both the boundary layer depth in Figure 8 and the tracer profiles in Figure 8. This shows that the most difficult cases are free convection and “weak wind, strong cooling”—the cases where convective dynamics dominate.

In the “weak winds, strong cooling” case, the 72-hr LES is forced by 156 W m^{-2} equivalent heat flux and 11 m s^{-1} 10-m atmospheric winds, while the 6-hr LES is forced by 1,666 W m^{-2} and 16 m s^{-1} 10-m winds. In the 6- and 12-hr cases, KPP exhibits a similar “stable stratification bias” as seen in free convection in Figure 5. SMC-LT exhibits a shallow bias for the strongly forced cases and a deep biased for the weakly forced cases (and quite accurate predictions for the 24-hr case). CATKE also predicts a too-sharp entrainment layer that is much thinner than the broad entrainment layer observed in the LES in the 6- and 12-hr weak winds, strong cooling cases. These simulations are farthest from quasi-equilibrium in time and may exhibit strong non-locality. Despite CATKE’s errors for the 6-hr case, however, CATKE’s boundary layer depth predictions for the 24-, 48-, and 72-hr case are accurate.

5.2.4. Constant Forcing Validation: Summary

CATKE exhibits less bias than either KPP or SMC-LT across all cases, even when making predictions “outside” its training data set. In particular, CATKE generates good predictions of boundary layer structure and depth, even in convective dominated cases where an analysis of tracer profiles suggests that CATKE tends to overmix. Fixing CATKE’s convective biases will likely require additional work with both the convective mixing length, and CATKE’s stability function formulation for $Ri < 0$.

CATKE makes good predictions relative to KPP or SMC-LT in part because its formulation expresses reasonable physical hypotheses, but also because its parameters have been calibrated comprehensively to minimize bias across a wide range of physical scenarios and vertical resolutions. In particular, the simulations that CATKE has been trained on are more similar to the extrapolation test cases (the 6- and 72-hr cases) than the data sets that either KPP or SMC-LT have been trained on. This generates ambiguity: do KPP and SMC-LT exhibit greater bias because of structural issues with their formulation, or do they need to be recalibrated in a similar manner as

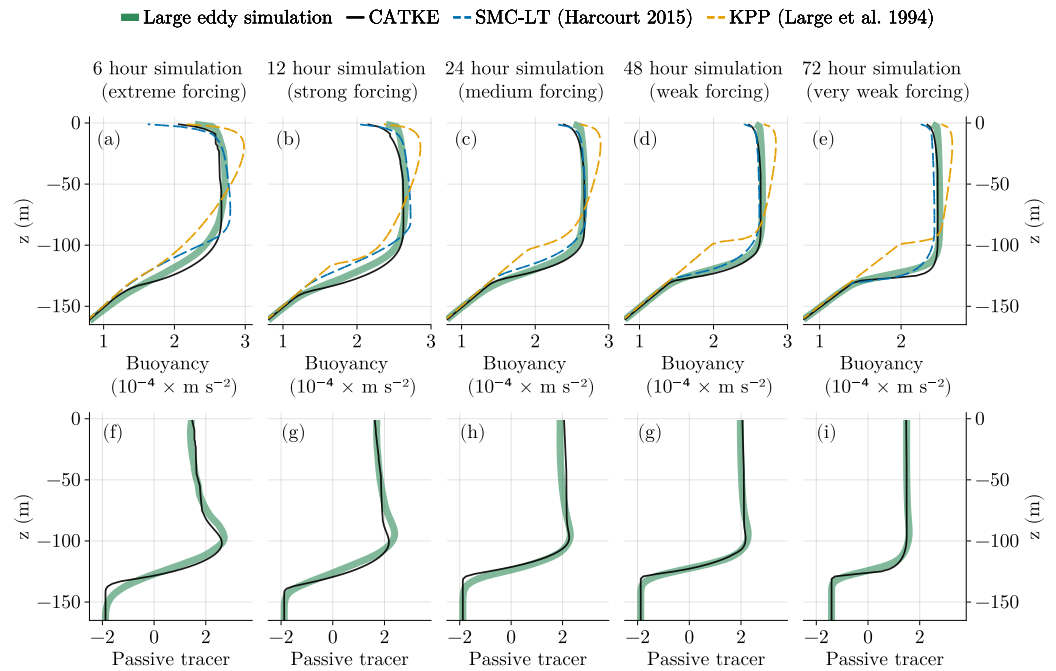


Figure 9. A four-way comparison between LES and three turbulence closures (CATKE, KPP, and SMC-LT) for the “mid wind, mid cooling” constant forcing cases described in Table 1 and Appendix A. The Coriolis parameter is $f = 10^{-4} \text{ s}^{-1}$, surface stresses correspond to 13–20 m s^{-1} 10-m winds, and surface cooling ranges from 125 to 1,333 W m^{-2} . See Figure 5.

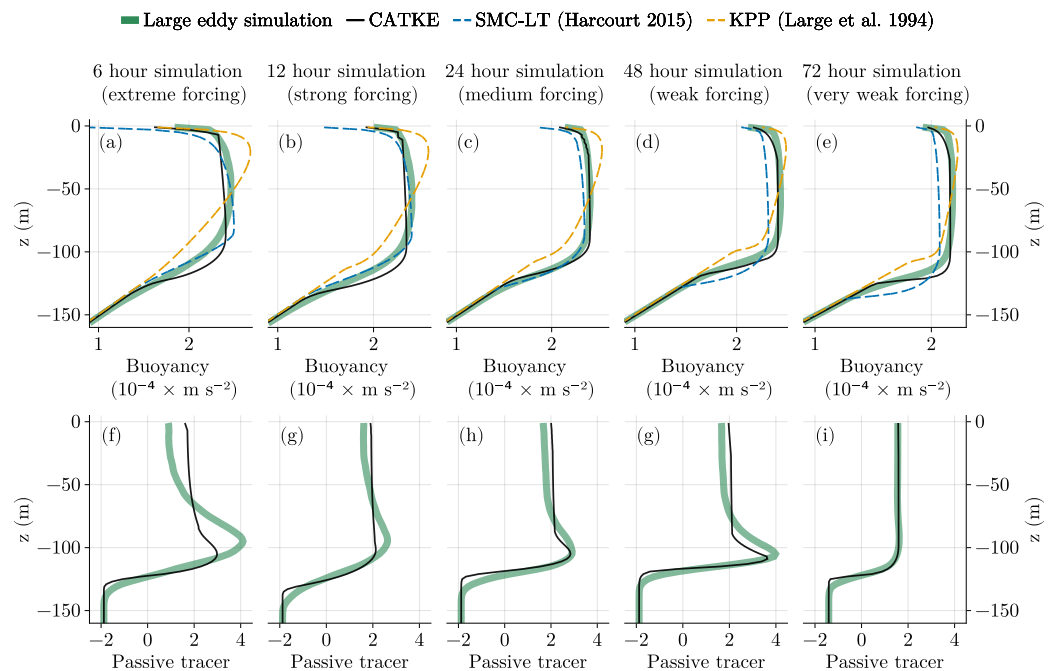


Figure 10. A four-way comparison between LES and three turbulence closures (CATKE, KPP, and SMC-LT) for the “weak wind, strong cooling” constant forcing cases described in Table 1 and Appendix A. The Coriolis parameter is $f = 10^{-4} \text{ s}^{-1}$, surface stresses correspond to 11–16 m s^{-1} 10-m winds, and surface cooling ranges from 156 to 1,666 W m^{-2} . See Figure 5.

CATKE? Answers prove elusive. While KPP has known structural biases (see, for example, Souza et al., 2020), the formulation of SMC-LT is seemingly more general than CATKE. Further understanding requires calibrating KPP and SMC-LT in the same way we calibrate CATKE.

5.3. Deep Cycle Turbulence in the Tropics

We turn to a validation case that requires significant extrapolation outside of the constant-forcing data set: 34 days of deep cycle turbulence in the tropics forced by time-varying winds, surface heat fluxes, and surface freshwater fluxes, as well as lateral flux divergences derived from a regional ocean model. The scenario and LES that we use to validate the single column model simulations are described by Whitt et al. (2022). A comparison between the same LES and two other turbulence closures is also given by Reichl et al. (2024).

Figure 11 illustrates the complex dynamics of this tropical turbulence situation by showing vertical kinetic energy from the LES, TKE from CATKE, and Ri from days 8–13 of the time-series. A combination of wind stress and stabilizing solar insolation in daytime produces a shallow, stably-stratified jet in the upper ~10 m of the water column. As day turns to night, outgoing radiation starts to dominate the incoming solar insolation to reduce stratification and eventually destabilize the upper part of the water column, producing turbulent mixing driven by a combination of convective buoyancy flux and shear. Momentum is thereby mixed downwards and injected into the stably stratified region below the base of the boundary layer. Remarkably, because the region below the boundary layer is close to marginally stable (Smyth & Moum, 2013), this nocturnal injection of momentum from above eventually leads to shear instability that spans the entire, roughly 100 m depth of the region below the mixed layer. More often than not, the turbulence “pulsates”—initial bursts of turbulence mix momentum and buoyancy, decay, and precipitate a second and even a third burst of turbulence later on the evening (Smyth et al., 2017). The process, which is called “deep cycle turbulence”, repeats itself the next day.

The slow growth and intermittent bursting of turbulence at night is prominent in LES vertical kinetic energy shown in Figure 11a. Figure 11b shows that CATKE exhibits a qualitatively similar bursting behavior, though the timing of the bursts are sometimes misrepresented. Moreover, inspection of Figures 11c and 11d reveals that CATKE underpredicts the Richardson number, Ri . (Panel d also shows that CATKE exhibits regions of negative Ri below $z = -70$ m which are absent from the LES. This deep unstable stratification, which can only be produced by the GCM-derived lateral flux divergences, is also present in other parameterizations, such as in the $k-\epsilon$ solutions that underpin Figures 13c and 14c. We are unsure why the lateral fluxes produce negative Ri , but do not investigate this issue further here. Finally, we note that this issue is relatively less prominent outside days 8–13 within the total 34 days time-series).

Figure 12 investigates the discrepancy between LES-derived and CATKE-based Ri further by plotting the median Ri , N^2 , and S^2 and shading the range of values between the 25% and 75% quantiles. The Ri statistics in the left panel show that while the LES Ri is relatively variable with a broad peak around $Ri \approx 0.21$, CATKE’s Ri are narrowly concentrated around its steady state value 0.18. Turning to N^2 (middle panel) and S^2 (right panel), we see that the Ri bias is not straightforwardly associated with a bias in either N^2 or S^2 —both are slightly over-predicted (indicating undermixing), but nevertheless exhibit similar medians and ranges compared to the LES.

Despite the errors in burst timing and Richardson number, CATKE’s predictions have realistic qualities not shared by other closures. To show this, Figures 13 and 14 compare the vertical temperature flux, and the time-derivative of the vertical temperature flux between the LES, CATKE, and the $k-\epsilon$ parameterization implemented in Oceananigans (Ramadhan et al., 2020; Umlauf & Burchard, 2005). $k-\epsilon$ is similar to SMC-LT except that, like the LES described by Whitt et al. (2022), it neglects surface wave effects. Note that the LES data has been smoothed with a moving average to reduce noise, which is especially distracting when computing the time derivative of the vertical flux.

In Figure 13, which shows the period between days 8–13, both the LES and CATKE vertical fluxes exhibit vertically-coherent bursts, whereas $k-\epsilon$ ’s flux predictions are smoother and smeared out over the deep turbulence cycle. The vertical coherence of vertical flux maxima is even more pronounced in the time-derivative of the vertical fluxes plotted in panels d–f. Figure 14 shows the same data between days 28–34, during which the three solutions are more qualitatively distinguished. In particular, the time-derivative of the $k-\epsilon$ fluxes shown in panel f of Figure 14 exhibit sharp, progressively deepening interfaces and generally lack vertically-coherent features. Neither the LES (panel d) or CATKE solutions (panel e) possess these interfaces and instead exhibit vertically-

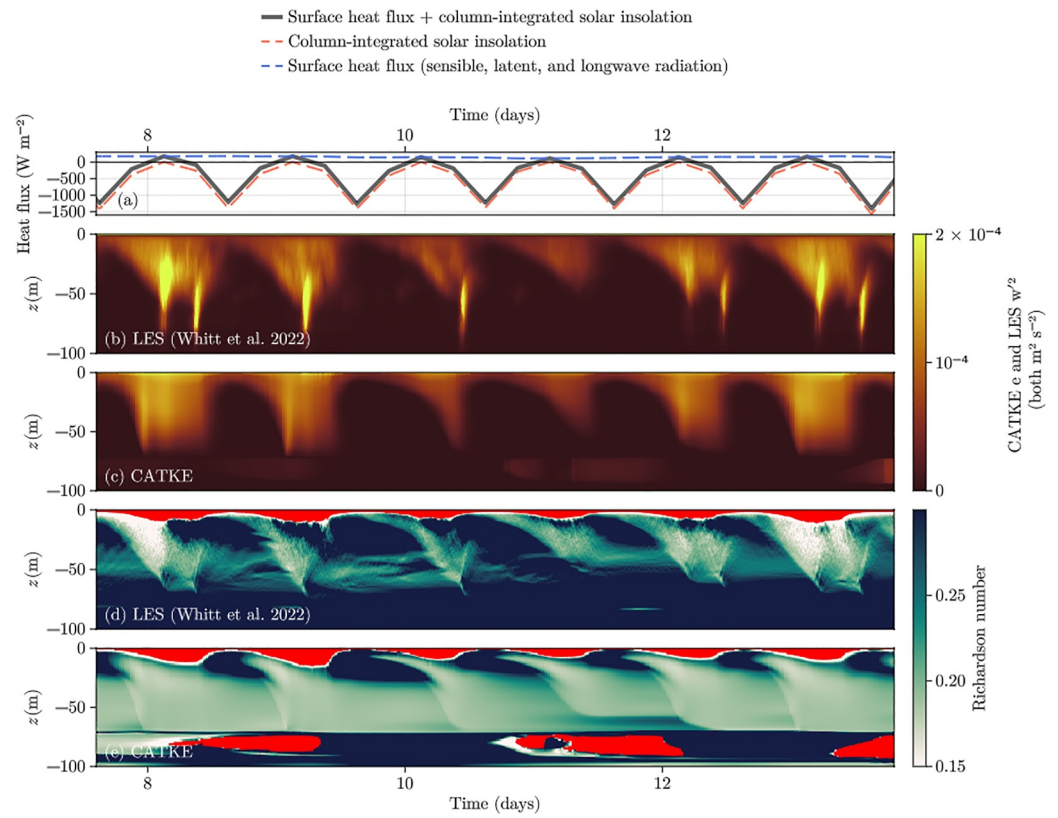


Figure 11. Overview of the tropical turbulence validation case. Panels show: (a) surface heat fluxes and solar insolation, (b) vertical kinetic energy $\overline{w'^2}$ from the LES described by Whitt et al. (2022), (c) CATKE's TKE variable, (d) the Richardson number computed from the horizontally-averaged LES momentum and buoyancy profiles, and (e) the Richardson number predicted by CATKE. The shaded red areas in panels (d) and (e) indicate a negative Richardson number. Shown here are days 8–13 out of the entire 34-day time-series. The heat fluxes are negative during the day (heat going downwards, into the ocean) and positive at night (heat going up, out of the ocean). The LES vertical kinetic energy and CATKE TKE exhibit intermittent bursting. In the deep region below the boundary layer where turbulent bursting occurs, LES-derived Richardson numbers get as low as 0.15. In the CATKE solution and in the same region, the Richardson number reaches a minimum of about 0.18.

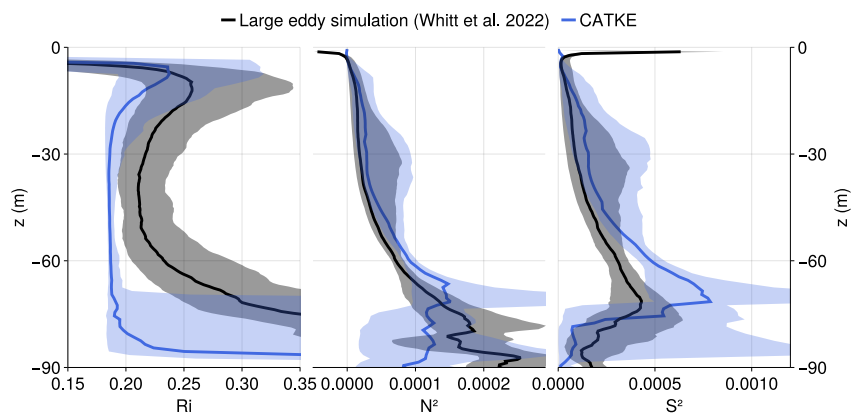


Figure 12. Median $Ri = N^2/S^2$ (left panel), and buoyancy frequency N^2 (middle), and shear S^2 (right panel) at each depth computed from 34 days of realistic equatorial turbulence simulated by LES and CATKE. The LES Ri is computed in terms of the horizontally-averaged shear and buoyancy. Shading shows the range between the 25% and 75% quantiles. CATKE's prediction of Ri is smaller and more narrowly distributed around its steady-state Richardson number $Ri^* = 0.18$ than the LES Ri . On the other hand, CATKE overpredicts both N^2 and S^2 , thus undermixing both momentum and buoyancy (with more momentum bias than buoyancy bias).

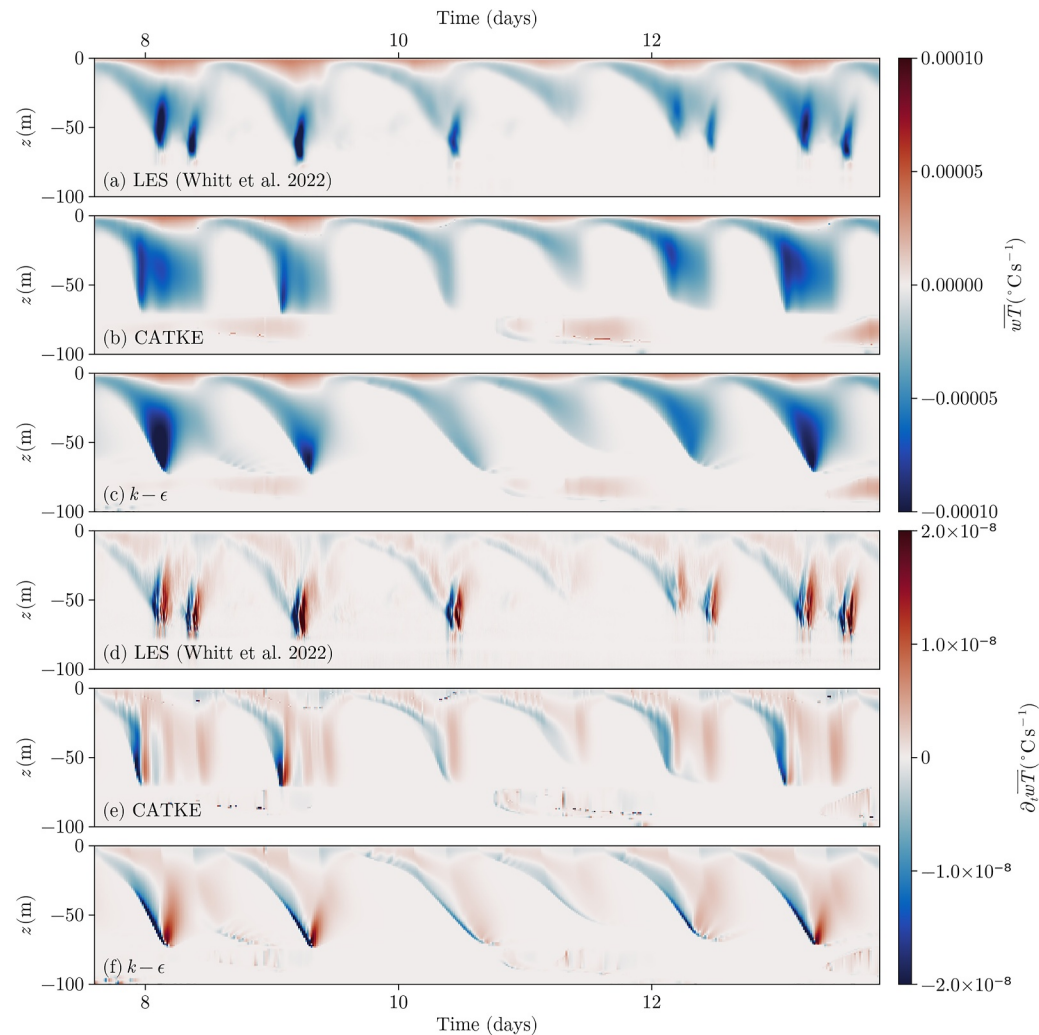


Figure 13. A comparison of the vertical temperature flux and vertical temperature flux divergence in tropical turbulence between LES (Whitt et al., 2022), CATKE, and the $k-\epsilon$ two-equation model (Umlauf & Burchard, 2005).

coherent features. Despite their qualitative similarity to LES, however, the CATKE solutions misrepresent the magnitude and timing of the vertically-coherent bursts. Improving both CATKE and $k-\epsilon$ will probably benefit from including time-dependent LES data with deep-cycle turbulence physics in a future calibration exercise.

5.4. Sensitivity to Vertical Resolution and Time-Step

Next we investigate the sensitivity of CATKE's predictions to numerical parameters like vertical resolution and time-step size—a well-appreciated concern with ocean microscale parameterizations (Reffray et al., 2015; Van Roekel et al., 2018). The sensitivity of CATKE's predictions to vertical resolutions ranging from 1 to 16 m is shown in Figure 15 for the weak wind, strong cooling case (the case for which CATKE exhibits the most bias). Recall that CATKE was calibrated using simulations with 2-, 4-, and 8-m vertical resolution, such that 1 and 16 m represent extrapolation in resolution. Based off the results in Figure 15, we conclude that CATKE is insensitive to vertical resolutions 8 m and finer. At 16 m resolution, CATKE's predictions are still better than KPP and SMC-LT, but nevertheless start to deviate from the higher-resolution CATKE solutions and, in particular, tend to overmix. It may be that with such a coarse resolution, the structure of strongly-stratified entrainment layers at the base of the boundary layer cannot be adequately resolved.

The sensitivity of CATKE's predictions to time-step size—at a vertical resolution of 1 m—are shown in Figure 16. Note that CATKE requires a smaller time step for finer vertical resolution. Put differently, smaller

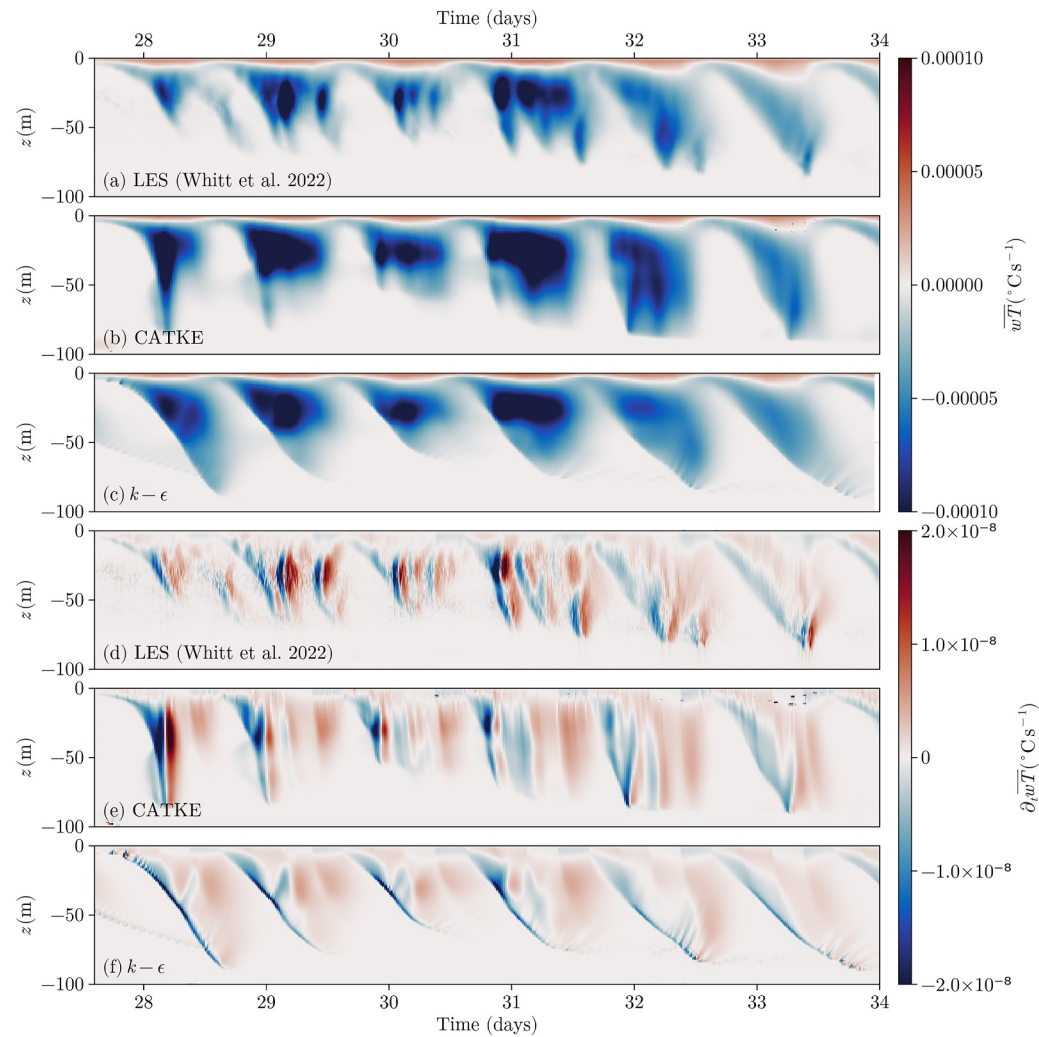


Figure 14. Vertical temperature flux and vertical temperature flux divergence as in Figure 13, but showing days 28–34.

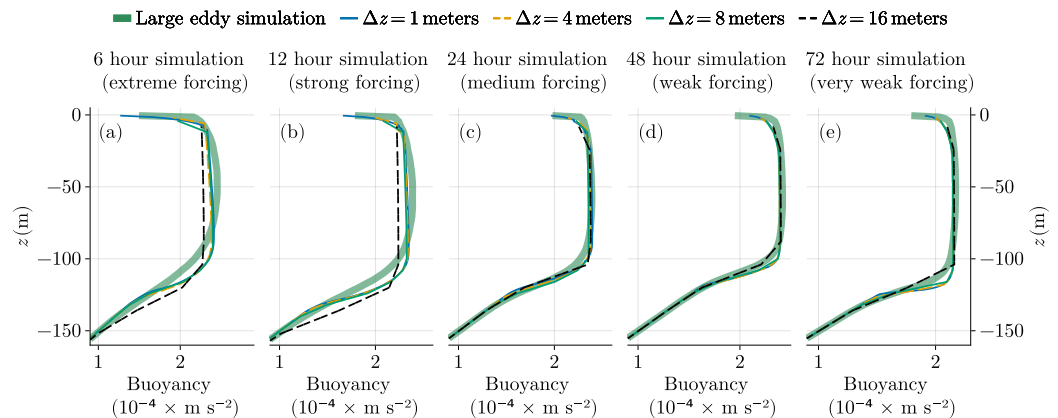


Figure 15. Illustration of sensitivity of CATKE predictions to vertical resolution for the weak wind, strong cooling case. Four vertical resolutions are shown: 1, 4, 8, and 16 m. CATKE’s calibration explicitly minimized errors between LES and CATKE simulations at 2, 4, and 8 m resolution, such that the 1 and 16 m cases represent “extrapolation in resolution.” The predictions are converged for resolutions 8 m and finer, but the 16 m resolution results exhibit small discrepancies from the converged solutions.

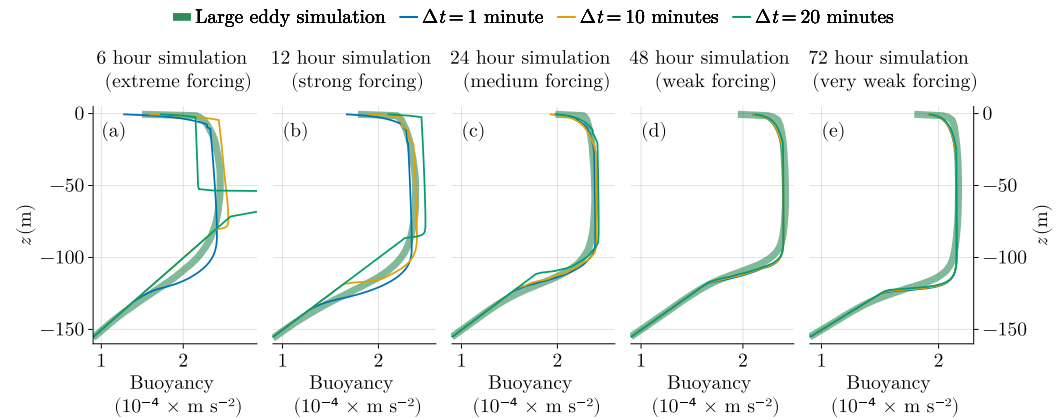


Figure 16. Sensitivity of CATKE predictions to time step for 1 m vertical resolution for the weak wind, strong cooling case. At 1 m resolution and in the strong forcing conditions of the 12- and 6-hr suites, CATKE solutions show time-step dependence for time steps longer than 1 min. To enable longer time steps for high vertical resolutions in the presence of strong forcing, the substepping scheme described in Appendix B is used and demonstrated in Figure 17.

time-steps are required to resolve the evolution of TKE, momentum, and tracers, and associated vertical transmission of information, on finer grids. More strongly forced cases also require smaller time steps. Figure 16, and additional tests, show that with 1 m vertical resolution, CATKE requires time-steps 2 min or shorter to resolve the dynamics associated with surface forcing as strong as that encountered in the 6-hr-suite. (A 5-min time step is adequately converged for the 12-, 24-, 48-, and 72-hr suite, however).

We address this sensitivity of CATKE's predictions to time-step by implementing a novel split-explicit scheme that substeps the TKE using a short time-steps, while evolving momentum and tracers with a longer time-step. The details are given in Appendix B. The results are shown in Figure 17, showing that CATKE generates converged predictions for momentum and tracer time-steps between 1 and 20 min when the TKE is substepped with a short 30 s time step. When using substepping, the TKE time-step can be configured according to the vertical resolution and strongest expected forcing over the duration of the simulation, while the momentum and tracer time-steps may be configured by other stability criteria, such as a Courant-Freiderichs-Lewy condition.

6. Discussion

This paper describes a novel one-equation parameterization for vertical fluxes by ocean microscale turbulence called "CATKE". CATKE extends existing one-equation parameterizations (Blanke & Delecluse, 1993; Madec

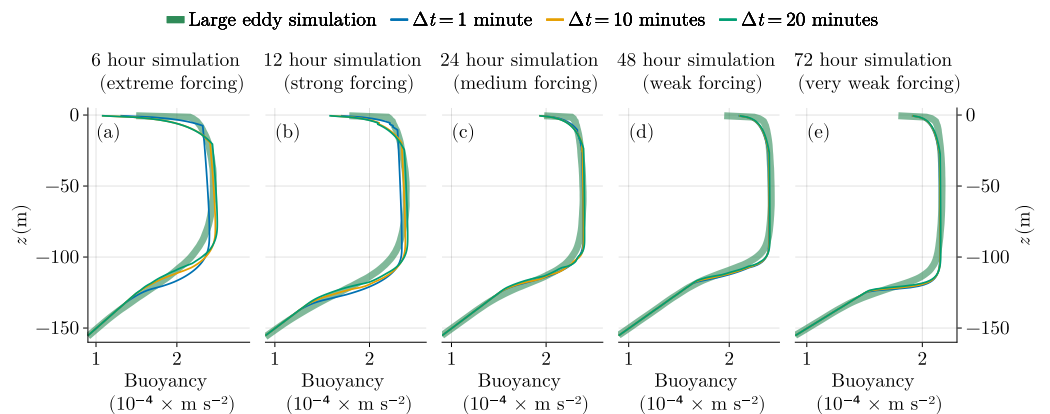


Figure 17. A comparison between LES and CATKE-parameterized single column simulations at 1 m vertical resolution and three different momentum and tracer time-steps, when turbulent kinetic energy (TKE) is substepped with a 30 s time step using the scheme described in Appendix B. For the 6-hr suite, the time-step dependence is greatly reduced compared to the non-substepped case shown in Figure 16, but is not entirely converged. We suspect this is because even momentum and tracers require a time step shorter than 20 min for such strong forcing at high vertical resolution.

et al., 2017) with a dynamic model for CA capable of describing the wide range of convective mixing rates observed in the ocean surface boundary layer. CATKE's 23 free parameters are calibrated against LESs accounting for discretization errors. We use a posteriori calibration, meaning that the CATKE parameters are calibrated to capture the full temporal evolution of the coarse-grained variables rather than, for example, matching the unresolved eddy fluxes. This approach improves both the accuracy and the stability of the calibrated parameterization.

Our decision to develop a one-equation TKE-based parameterization rather than a K -profile parameterization (KPP, see Large et al., 1994; McWilliams et al., 2009; Van Roekel et al., 2018; Reichl & Hallberg, 2018; Reichl & Li, 2019) merits some discussion. KPPs have a major advantage over TKE-based parameterizations in coarse resolution ocean models (especially with different time-steps for momentum and tracer variables) because they admit time-steps as long as 2 hr (Reichl & Hallberg, 2018). In part, we are interested in one-equation parameterization because our focus is higher resolution, mesoscale-permitting and mesoscale-resolving simulations that require 1–10 min time-steps to satisfy the advective numerical stability constraints of energetic solutions on relatively high-resolution grids. CATKE adds no additional time step constraints to such simulations, while offering some significant benefits: (a) dynamic prediction of diffusivity vertical structure versus prescription via “shape functions”; (b) turbulent intensity growth and relaxation time scales or “memory”, and (c) better computational performance on hardware with fine-grained parallelism such as GPUs used for example, by Oceananigans (Ramadhan et al., 2020; Silvestri, Wagner, Constantinou, et al., 2024) and Veros (Häfner et al., 2021), which are ill-suited for the nonlinear solvers for boundary layer depth common to KPP-type models (Zhang et al., 2020).

The automated calibration described in Section 4 and Appendix C was repeated hundreds of times during the development of CATKE. We developed CATKE by starting with a simple formulation similar to the one described by Blanke and Delecluse (1993)—with no stability functions (and thus a constant Prandtl number) and no special convective mixing length. We then progressed, using calibration to justify increasing model complexity, to the presently described form with continuously Ri -dependent stability functions in Equation 28 and the convective mixing length described in Section 3.1.5. This development process represents a “knowledge discovery loop” (National Academies of Sciences et al., 2022) with three steps: (a) formulation, (b) calibration, and (c) assessment. For complex, nonlinear models—and even in the relatively simple single column context of this paper—automatic calibration is essential to progress quickly from formulation to assessment, and then to discover and justify further improvements to formulation, thereby iteratively producing a high-quality, well-motivated, parsimonious parameterization.

Our calibration to a relatively limited range of LES cases reported in this paper (though extensive compared prior efforts in ocean turbulence parameterization development) is just the first step toward using CATKE for global ocean modeling and climate projection. In particular, our ultimate objective is more accurate climate predictions with quantified uncertainties. Addressing this ultimate goal requires first quantifying the uncertainty of CATKE's free parameters relative to LES, using the calibration context presented in this work. Next, with prior parameter distributions in hand, CATKE's free parameters must then be recalibrated concomitant with other climate model free parameters against global climate observations to account for physics missing from the LES in this work, and to account for interactions between CATKE and other components of the climate model.

A second future step is to further calibrate CATKE to a more comprehensive suite of LES forced with temporally-varying surface fluxes, surface wave fields with $La \neq 0.3$, and horizontal flux divergences (e.g., following Whitt et al., 2022). These calibrations against more comprehensive LES will provide better prior estimates of CATKE's parameters in preparation of the final goal of calibrating CATKE in a global context. More comprehensive calibration to more LES and to observations in a global context will likely reveal deficiencies to be addressed by further development of CATKE's formulation, such as accounting for the effect of surface waves on CATKE's mixing and dissipation length scales.

Appendix A: A Synthetic DataSet Generated by Large Eddy Simulations

We use a synthetic data set to calibrate and assess CATKE consisting of 35 idealized large eddy simulations (LES) of the ocean surface boundary layer with imposed constant surface fluxes of temperature and momentum and a simple surface wave field.

A1. Initial Conditions

The LES are initialized from rest with zero velocity and the piecewise-linear buoyancy stratification

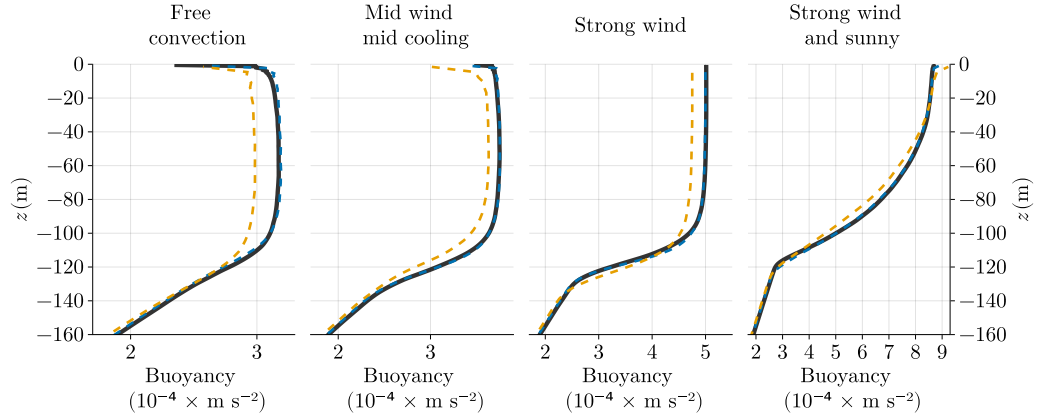


Figure A1. Resolution dependence of 12-hr LES.

$$b(z, t=0) = \begin{cases} N_1^2 z & \text{for } z > -h_1, \\ N_2^2 z + (N_2^2 - N_1^2) h_1 & \text{for } -h_2 < z < -h_1, \\ N_3^2 z + (N_3^2 - N_2^2) h_2 + (N_2^2 - N_1^2) h_1 & \text{for } z < -h_2, \end{cases} \quad (\text{A1})$$

with $N_1^2 = N_3^2 = 2 \times 10^{-6} \text{ s}^{-2}$, $N_2^2 = 10^{-5} \text{ s}^{-2}$, $h_1 = 48 \text{ m}$, and $h_2 = 72 \text{ m}$.

A2. Passive Tracer Forcing

We additionally simulate the evolution of a passive tracer c which is forced by

$$F_c(z) = \omega_+ e^{-(z-z_c)^2/2\lambda_c^2} - \omega_-, \quad (\text{A2})$$

where z_c is the depth of the forcing, λ_c is the width of the forcing, ω_+ is an inverse forcing time-scale that varies between each suite, and ω_- is chosen so that F_c has zero mean, that is

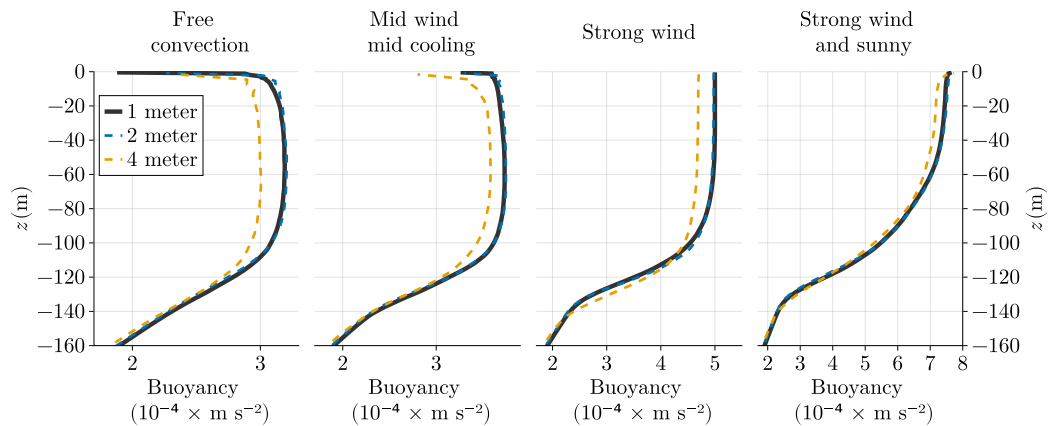


Figure A2. Resolution dependence of 24-hr LES.

$$\omega_- \stackrel{\text{def}}{=} \frac{\omega_+}{L_z} \int_{-L_z}^0 e^{-(z-z_c)^2/2\lambda_c^2} dz \quad (\text{A3})$$

$$\approx \omega_+ \frac{\lambda_c \sqrt{2\pi}}{L_z}, \quad (\text{A4})$$

where L_z is the depth of the domain. The approximation in A4 holds when the forcing is far from boundaries, or when $-L_z \ll z_c - \lambda_c$ and $0 \gg z_c + \lambda_c$.

To generate tracer gradients within the boundary layer, we use a relatively narrow forcing profile with $\lambda_c = 8$ m centered at $z_c = -96$ m, near the bottom of the boundary layer at the end of each simulation. We additionally use a forcing time scale ω_+^{-1} that is similar to the typical mixing time-scale: 15 min, 30 min, 1 hr, 2 hr, and 4 hr for the 6, 12, 24, 48, and 72 hr suites, respectively. These choices ensure a passive tracer profile that, unlike the well-mixed buoyancy profile, reveals the structure of turbulent tracer mixing within the boundary layer. The passive tracer data thus provides an important additional constraint on CATKE's prediction of the tracer mixing length, ℓ_c .

A3. Constant-Flux Boundary Conditions

The 35 simulations, which have different boundary conditions and Stokes drift are organized into 5 “suites”, each of which has 7 cases: free convection, weak wind strong cooling, medium wind medium cooling, strong wind weak cooling, strong wind, strong wind no rotation, and strong wind and sunny. The suites differ by both forcing strength and duration, simulating 6, 12, 24, 48, and 72 hr of boundary layer turbulence respectively. The forcing strength is chosen for each suite and case so that the boundary layer deepens to roughly half the depth of the domain; for example, the “6-hr suite” has the strongest forcing, and the “72-hr suite” has the weakest forcing. “Strong wind no rotation” and “strong wind and sunny” use $f = 0$, while the rest use the Coriolis parameter $f = 10^{-4} \text{ s}^{-1}$. The surface fluxes for the 35 LES are summarized in Tables 1 and 2. To draw a connection between the LES suites and real air-sea flux conditions, Tables 1 and 2 provide an estimate of heat fluxes Q for each case, as well as an estimate of the atmospheric wind at 10 m height using similarity theory (reduced to the case of neutral buoyancy fluxes for simplicity, see Large and Yeager (2009)),

$$u_{10} = \sqrt{\frac{|\tau_a|}{c_{10}}}, \quad \text{where } c_{10} = \left(\frac{\kappa}{\log(10/\ell_r)} \right)^2, \quad \text{and } \ell_r = 0.011 \frac{|\tau_a|}{g}, \quad (\text{A5})$$

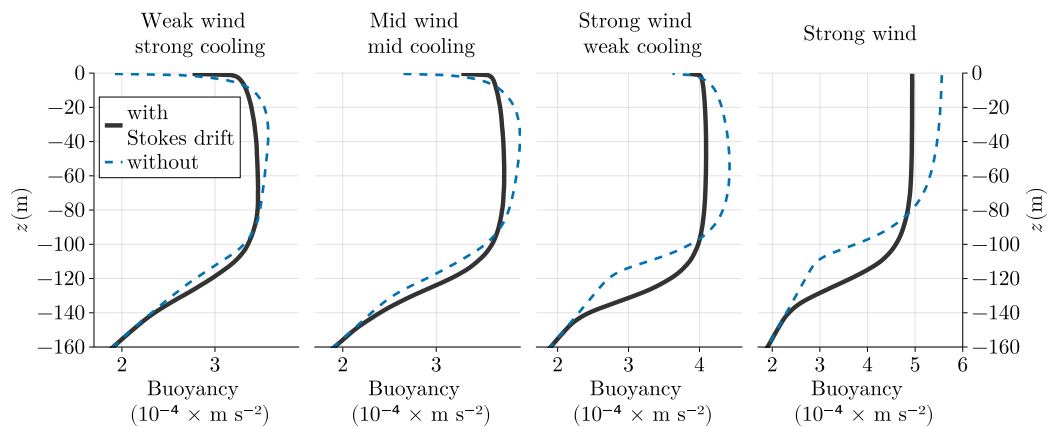


Figure A3. Stokes drift dependence of 12-hr LES.

where ℓ_r is the Charnock roughness length given gravitational acceleration $g = 9.81 \text{ m s}^{-2}$, $\kappa = 0.4$ is the von Kármán constant, and $\tau_a = \rho_o \tau_x / \rho_a$ is the atmospheric kinematic momentum flux given ocean reference density $\rho_o = 1024 \text{ kg m}^{-3}$ and atmosphere density $\rho_a = 1.2 \text{ kg m}^{-3}$.

A4. Stokes Drift Model

For all wind-forced cases, we additionally impose a surface wave field with a surface Stokes drift amounting to a constant “Langmuir number” $La = \sqrt{u_\star / U^S(z=0)} \approx 0.3$. Our Stokes drift prescription models a surface wave field with the friction-number-dependent peak wavenumber

$$k_p = C_k \frac{g}{u_\star^2}, \quad (\text{A6})$$

where $u_\star = \sqrt{|\tau_x|}$ is the water-side friction velocity, g is gravitational acceleration, and we use $C_k = 10^{-6}$.

We follow Lenain and Pizzo (2020) to estimate the depth-profiles of Stokes drift and Stokes drift shear. The Stokes drift beneath a spectrum of deep-water waves is

$$U^S(z) = 2 \int_{k_p}^{k_i} e^{2kz} k \sqrt{gk} \chi(k) dk, \quad (\text{A7})$$

where $\chi(k)$ is a one-dimensional wave spectrum that neglects “directional spreading”. The spectrum $\chi(k)$ is divided into an “equilibrium range” just above the spectral peak k_p , and a “saturation range” at even higher wavenumbers:

$$\chi(k) = \begin{cases} \frac{C_\beta}{2\sqrt{g}} a_\star k^{-5/2} & \text{for } k_p < k < k_n \text{ (equilibrium)}, \\ C_B k^{-3} & \text{for } k_n < k < k_i \text{ (saturation)}, \end{cases} \quad (\text{A8})$$

where k_n is a transition wavenumber between equilibrium and saturation ranges, k_i is an upper wavenumber cutoff above which waves are assumed to be isotropic and there do not contribute to Stokes drift. $a_\star = u_\star \sqrt{\rho_o / \rho_a}$ is the air-side friction velocity defined in terms of the water-side friction velocity u_\star , a reference air density $\rho_a = 1.2 \text{ kg m}^{-3}$ and ocean density $\rho_o = 1024 \text{ kg m}^{-3}$. Wavenumbers below the spectral peak k_p are assumed too weak to contribute appreciably to Stokes drift.

Both the transition wavenumber k_n and the isotropic wavenumber k_i decrease with increasing u_\star :

$$k_n \stackrel{\text{def}}{=} C_r g a_\star^{-2}, \quad (\text{A9})$$

$$k_i \stackrel{\text{def}}{=} C_i g a_\star^{-2}, \quad (\text{A10})$$

where $C_r = 9.7 \times 10^{-3}$ and $C_i = 0.072$.

The Stokes drift is

$$U^S(z) = C_\beta a_\star \int_{k_p}^{k_n} \frac{e^{2kz}}{k} dk + 2C_B \sqrt{g} \int_{k_n}^{k_i} k^{-3/2} e^{2kz} dk. \quad (\text{A11})$$

Noting that $\int_{k_p}^{k_n} k^{-1} e^{2kz} dk = \text{Ei}(2k_n z) - \text{Ei}(2k_p z)$, where Ei is the exponential integral function, we find

$$U^S(z) = C_\beta a_\star [\text{Ei}(2k_n z) - \text{Ei}(2k_p z)] + 2C_B \sqrt{2gkz} [v(2k_n z) - v(2k_i z)], \quad (\text{A12})$$

where

$$v(\zeta) = \frac{2}{\zeta} \left[e^{\zeta} + \sqrt{\pi|\zeta|} \operatorname{erf}(\sqrt{|\zeta|}) \right],$$

and

$$\partial_z U^S = 2C_\beta a_\star \int_{k_p}^{k_n} e^{2kz} dk + 4C_B \sqrt{g} \int_n^l \frac{e^{2kz}}{\sqrt{k}} dk, \quad (\text{A13})$$

$$= C_\beta a_\star \frac{e^{2k_p z} - e^{2k_n z}}{|z|} + 2C_B \sqrt{\frac{2\pi g}{|z|}} \left[\operatorname{erf}(\sqrt{2k_n |z|}) - \operatorname{erf}(\sqrt{2k_l |z|}) \right], \quad (\text{A14})$$

for the Stokes shear.

A5. LES Uncertainty: Effects of Resolution and Stokes Drift

All LES use 2 m horizontal resolution and a stretched vertical resolution that varies from 0.8 m in the upper half of domain to 2.3 m at the bottom. We refer to this as “1 m” vertical resolution. Our LES utilize an “implicit” model for subgrid fluxes whereby kinetic energy and tracer variance are solely dissipated by a minimally-diffusive 9th-order WENO advection scheme (Shu, 2020). The advantages of using WENO-based implicit dissipation (and no explicit closure for subgrid turbulent fluxes) are discussed by Pressel et al. (2017) and Silvestri, Wagner, Campin, et al. (2024).

To account for the effects of resolution on the 35 LES used as synthetic observations in this paper, we run 70 additional LES on coarser grids with double (“2 m”) and quadruple (“4 m”) resolution, and use these to estimate the observational uncertainty used in calibration (see 4 for more details). The effect of resolution depends on forcing strength: for the 6 and 12 hr suite, the results are nearly identical for 1- and 2-m vertical resolution. Figure A1 shows the results for 4 cases in the 12 hr suite. Note that in the free convection case, the first two grid points exhibit a strong unstable stratification in the 12 hr suite. We attribute this to an artificial reduction of mixing near the top boundary of the LES. It might be possible to address this artificially-strong unstable mean stratification by introducing, for example, a surface-concentrated eddy diffusivity. However, because the LES are used only for training CATKE and thus matter mostly in their predicted boundary layer depth, we choose instead to ignore the top 4 m when computing the LES–CATKE discrepancy during calibration.

Figure A2 shows the resolution dependence of the 24-hr suite. These LES show slightly more resolution dependence than the 12-hr suite, especially for cases forced by a combination of wind and cooling. This indicates that our LES data for more weakly forced cases are *less certain* than the strongly forced cases.

A6. Effect of Stokes Drift on LES Results

Next we turn to the effect that including the Stokes drift profile described in section A4 has on our LES results. The inclusion of Stokes drift in our LES is an attempt to make them slightly more realistic. In other words, we hypothesize that calibrating CATKE to LES without surface waves would generally lead to a shallow bias in mixed layer depth prediction with CATKE—since surface waves are always present above real wind-forced ocean surface boundary layers.

This notion is corroborated by Figure A3, which shows the horizontally-averaged buoyancy profiles for 4 LES in the 12 hr suite, with and without Stokes drift. As expected, the inclusion of Stokes drift produces more mixing and makes the boundary layer deeper. The effect of Stokes drift is minor in the case of weak and medium winds (leftmost and second from left panels). In the strong wind (and rotating) case, the inclusion of Stokes drift makes the boundary layer 20 m deeper, or around 20% of the total. In the strong wind, no rotation case, the case without Stokes drift completely fails to transition to the turbulence. (A small amount of cooling would probably be required to produce turbulence in the strong wind, no rotation case without Stokes drift).

Appendix B: Split-Explicit Turbulent Kinetic Energy Time Stepping and Vertical Discretization

CATKE's time discretization is a little non-trivial since we step forward velocity and tracers first, then step forward TKE and also use substepping/split-explicit scheme for TKE. In the single column case, we integrate Equations 13–15 with the backward Euler scheme

$$\frac{u^{n+1} - u^n}{\Delta t} = \partial_z (K_u^n \partial_z u^{n+1}) + f v^n + \bar{F}_u^n, \quad (\text{B1})$$

$$\frac{v^{n+1} - v^n}{\Delta t} = \partial_z (K_v^n \partial_z v^{n+1}) - f u^n + \bar{F}_v^n, \quad (\text{B2})$$

$$\frac{c^{n+1} - c^n}{\Delta t} = \partial_z (K_c^n \partial_z c^{n+1}) + \bar{F}_c^n, \quad (\text{B3})$$

where $\Delta t = t^{n+1} - t^n$ and the superscripts n or $n + 1$ indicate the time step at which the quantity is evaluated. For the TKE Equation 19, we introduce a substepping scheme that uses M short time step sizes $\Delta t/M$ to integrate e between n to $n + 1$,

$$\frac{e^{m+1} - e^m}{\Delta t/M} = \underbrace{\partial_z (K_e^m \partial_z e^{m+1})}_{\text{transport}} + \underbrace{K_u^n \frac{1}{2} (\partial_z u^n + \partial_z u^{n+1}) \cdot \partial_z u^{n+1}}_{\text{shear production}} + \overline{w' b'^m} - \underbrace{\frac{\sqrt{e^m}}{\epsilon_D^m} e^{m+1}}_{\text{dissipation}}, \quad (\text{B4})$$

where the superscripts m and $m + 1$ denote the substep level. In practice, when using substepping, we fix the time step size for the TKE equation, Δt_e , and compute the substep number $M = \text{ceil}(\Delta t / \Delta t_e)$ in terms of Δt_e and the momentum and tracer time step size, Δt .

The buoyancy flux $\overline{w' b'^m}$ in B4 is discretized in time using the conditionally-implicit “Patankar trick” (Burchard, 2002), such that

$$\overline{w' b'^m} = \begin{cases} -K_c^n \partial_z b^{n+1} & \text{when } \partial_z b^{n+1} \leq 0 \\ -K_c^n \partial_z b^{n+1} \frac{e^{m+1}}{e^m} & \text{when } \partial_z b^{n+1} > 0 \end{cases} \quad (\text{B5})$$

which improves the stability of B4 and keeps e from becoming too negative due to numerical errors associated with, for example, advection schemes with oscillatory errors. Note that shear production is not updated during substepping. The time discretization of the shear production term in B4, which incorporates shear measured at the time step n and $n + 1$, also follows Burchard (2002) and requires an algorithm that stores the velocity field at time step n , stepping forward momentum and tracers, and then substepping forward e .

We spatially-discretize u , v , c , and e on a staggered vertical grid (not shown), with all variables vertically located at cell centers—a deviation from Blanke and Delecluse (1993), Burchard (2002), or Madec et al. (2017) who place u, v, c at vertical cell centers but TKE at vertical cell interfaces where the diffusivity is computed (sometimes called “ w -locations”). The vertical spatial discretization of the shear production term is derived from the mean kinetic energy equation following Burchard (2002), but adapted to our cell-centered placement of e . We use a tridiagonal solve to advance u, v, c, e in B1–B4 over each time step of substep, treating both diffusion and linear terms in B4 implicitly.

Discretizing e at cell centers allows us to re-use tracer advection and diffusion schemes and may yield a higher-quality representation of three-dimensional advection (a process that is neglected in the single column results of this paper). However, we anticipate a trade-off between representing advection and the need to reconstruct e to compute the diffusivities K_u , K_c , and K_e at vertical cell interfaces according to 12. That said, the vertical

resolution results shown in Figure 15 suggest that our discretization yields accurate solutions at 10-m-resolution and finer. We leave further investigation into CATKE's vertical discretization (which may depend on the application, since for example the advection of e likely only becomes important at very high horizontal resolution) for future work.

Appendix C: A Posteriori Calibration

We use Ensemble Kalman Inversion (EKI; Iglesias et al., 2013) to calibrate CATKE. EKI is a gradient-free and computationally inexpensive method for solving nonlinear inverse problems. EKI supposes that a forward map $\mathcal{G}(\mathbb{C})$ can predict uncertain observations \mathcal{Y} given a set of free parameters \mathbb{C} ,

$$\mathcal{Y} = \mathcal{G}(\mathbb{C}) + \eta, \quad (\text{C1})$$

where $\eta \sim \mathcal{N}(0, \mathcal{M})$ is normally-distributed random uncertainty with covariance \mathcal{M} . Four objects appear in the model-data relation (C1),

1. *Observations* \mathcal{Y} with Q discrete elements \mathcal{Y}_q . In this paper, each \mathcal{Y}_q represents a state variable like velocity U or buoyancy B at a particular depth and time, computed from LES data by horizontal averaging and vertical coarse-graining, and then normalized and shifted to have zero mean and unit variance.
2. A *parameter set* \mathbb{C} with P free parameter values \mathbb{C}_p .
3. A *forward map* $\mathcal{G}(\mathbb{C})$ whose elements $\mathcal{G}_q(\mathbb{C})$ predict the observation \mathcal{Y}_q . $\mathcal{G}(\mathbb{C})$ represents a *model* that maps a parameter set \mathbb{C} to the space of observations \mathcal{Y} . In our case, constructing $\mathcal{G}(\mathbb{C})$ requires forward evaluations of 63 single column models parameterized by \mathbb{C} , each predicting the evolution of horizontally-averaged variables in 21 LES at 2-, 4-, and 8-m resolution.
4. Random Gaussian *uncertainty* $\eta \sim \mathcal{N}(0, \mathcal{M})$ with covariance \mathcal{M} associated with both $\mathcal{G}_q(\mathbb{C})$ and \mathcal{Y}_q . η conflates uncertainty in \mathcal{Y} with “structural” uncertainty associated with imperfect forward maps \mathcal{G} .

The elements of \mathcal{Y} are the discrete values of the horizontally-averaged temperature and velocity fields output from 21 LES coarse-grained to three grids with uniform 2-, 4-, and 8-m spacing. Each physical field is shifted, normalized, and weighted before being assembled into \mathcal{Y} . Each forward map $\mathcal{G}(\mathbb{C})$ involves $3 \times 21 = 63$ simulations to find U , V , and B profiles for each LES case at the three model vertical resolutions.

C1. Ensemble Kalman Dynamics

Ensemble Kalman Inversion may be interpreted as a dynamical system that governs the evolution of an ensemble of E parameter sets, or “particles”, $\mathbb{C} \stackrel{\text{def}}{=} [\mathbb{C}^1, \mathbb{C}^2, \dots, \mathbb{C}^E]$. Here the superscript α denotes the “particle index”, which varies across the ensemble: \mathbb{C}_p^α is the p^{th} parameter value of the α^{th} particle.

Each parameter set \mathbb{C}^α obeys the ordinary differential equation

$$\frac{d}{d\mathcal{T}} \mathbb{C}^\alpha = -\mathcal{K}(\mathbb{C}, \mathbf{G}) \mathcal{M}^{-1} (\mathcal{G}^\alpha - \mathcal{Y}), \quad (\text{C2})$$

where $\mathcal{G}^\alpha \stackrel{\text{def}}{=} \mathcal{G}(\mathbb{C}^\alpha)$ is the forward map computed with the parameter set \mathbb{C}^α , and \mathcal{T} is the “pseudotime”. The matrix $\mathcal{K}(\mathbb{C}, \mathbf{G})$ in (C2) is the covariance matrix estimated from ensemble statistics at pseudotime \mathcal{T} , thus coupling the evolution of the ensemble. For two “ensemble matrices” \mathbf{A} and \mathbf{B} , where \mathbf{A} for example, is constructed from an ensemble of vectors $[A_i^1, A_i^2, \dots, A_i^E]$, the elements $\mathcal{K}_{ij}(\mathbf{A}, \mathbf{B})$ are defined

$$\mathcal{K}_{ij}(\mathbf{A}, \mathbf{B}) \stackrel{\text{def}}{=} \frac{1}{N} \sum_{\alpha=1}^N (A_i^\alpha - \langle A \rangle_i) (B_j^\alpha - \langle B \rangle_j), \quad \text{with} \quad \langle C \rangle_i \stackrel{\text{def}}{=} \frac{1}{E} \sum_{\alpha=1}^E C_i^\alpha. \quad (\text{C3})$$

For nearly-linear maps $\mathcal{G}_q(\mathbb{C}) \approx H_{pq} \mathbb{C}_p$, C2 reduces to

$$\frac{d}{d\mathcal{T}} \mathbb{C}^\alpha \approx -\mathcal{K}(\mathbb{C}, \mathbb{C}) \nabla_{\mathbb{C}} \Phi^\alpha, \quad (\text{C4})$$

where $\mathcal{K}_{ij}(\mathbb{C}, \mathbb{C})$ is the $P \times P$ parameter-parameter covariance matrix (Kovachki & Stuart, 2019). The “EKI objective” Φ^α associated with parameter set α appears in C4, where

$$\Phi(\mathcal{G}, \mathcal{Y}; \mathbb{C}) \stackrel{\text{def}}{=} \left\| \mathcal{M}^{-1/2} [\mathcal{G}(\mathbb{C}) - \mathcal{Y}] \right\|^2, \quad (\text{C5})$$

and $\Phi^\alpha \stackrel{\text{def}}{=} \Phi(\mathcal{G}, \mathcal{Y}; \mathbb{C}^\alpha)$. Φ in C5 is a functional of \mathcal{G} that measures the uncertain discrepancy between $\mathcal{G}(\mathbb{C}) - \mathcal{Y}$. The system C4 minimizes Φ using gradient descent preconditioned with $\mathcal{K}(\mathbb{C}, \mathbb{C})$, where the gradients $\nabla_{\mathbb{C}} \Phi$ are estimated from the parameter ensemble.

We integrate the EKI dynamical system C2 in using a forward Euler discretization,

$$\mathbb{C}^\alpha|_{\nu+1} = \mathbb{C}^\alpha|_{\nu} - \Delta\mathcal{T} [\mathcal{K}(\mathbb{C}, \mathbb{G}) \mathcal{M}^{-1} (\mathcal{G}^\alpha - \mathcal{Y})]_{\nu}, \quad (\text{C6})$$

where ν is the pseudotime iteration and $\Delta\mathcal{T}$ is a pseudotime step size. The adaptive step size $\Delta\mathcal{T}$ is chosen at each iteration according to Kovachki and Stuart (2019). The initial parameter sets \mathbb{C}^α at $\mathcal{T} = 0$ are generated by randomly sampling the priors listed in table 3.

EKI is practical for two reasons: (a) it does not require explicit gradients of \mathcal{G} with respect to parameters \mathbb{C} , and (b) the forward map evaluations \mathcal{G}^α —the most expensive part of integrating C2—are independent and thus easily parallelized. Reason (a) means EKI is applicable to any simulation framework with changeable parameters \mathbb{C} . Reason (b) means that considerable yet distributed resources can be leveraged efficiently: given sufficient distributed resources, the cost of a single EKI iteration depends only on the cost of a single forward map evaluation, independent of ensemble size. This parallelizability benefits small problems such as calibration in a single column context.

C2. Uncertainty Covariance

We associate the uncertainty \mathcal{M} with the numerical fidelity of the LESs by defining

$$\mathcal{M} = \text{cov}([\mathcal{Y}^{1m} \mathcal{Y}^{2m} \mathcal{Y}^{4m}]), \quad (\text{C7})$$

where $\mathcal{Y}^{1m}, \mathcal{Y}^{2m}, \mathcal{Y}^{4m}$ denote observations obtained from LES with 1-, 2-, and 4-m vertical resolution.

C3. Constrained and Unconstrained Parameters

The dynamics C6 require normally-distributed parameters \mathbb{C}_p , which precludes the imposition of strict bounds such as non-negativity. We therefore introduce the forward and inverse transforms,

$$\mathbb{C}_p = \log \frac{b - \tilde{\mathbb{C}}_p}{\tilde{\mathbb{C}}_p - a} \quad \text{and} \quad \tilde{\mathbb{C}}_p = a + \frac{b - a}{1 + \exp(\mathbb{C}_p)}, \quad (\text{C8})$$

between “constrained” physical parameters $\tilde{\mathbb{C}}$ that are bounded between (a, b) , and unconstrained parameters \mathbb{C} . The transformation C8 implies that if \mathbb{C}_p is normally-distributed then $\tilde{\mathbb{C}}$ is bounded by (a, b) with a scaled, shifted logit-normal distribution.

We denote the scaled, shifted logit-normal distribution bounded by (a, b) as $\mathcal{B}(a, b)$ and use it to model the distribution of all of CATKE’s free parameters. The distributions $\mathcal{B}(a, b)$ formulated so their corresponding normal distributions have zero mean and unit variance. When integrating C6, the normally-distributed parameter sets \mathbb{C}^α are transformed into their physical space counterparts $\tilde{\mathbb{C}}^\alpha$ via C8 when evaluating $\mathcal{G}^\alpha = \mathcal{G}(\mathbb{C}^\alpha)$ and thus solving the single column Equations 13–15 and 19.

C4. Failure Criterion Handling

Poor parameter choices \mathcal{C}^α often lead to failed simulations of the single column system 13–15 and 19. In that case the forward map \mathcal{G}^α is not informative and must be ignored when performing the Euler step C6.

We first define the median and the “median absolute deviation” of the EKI objective samples, $\Phi^{\alpha\text{def}} = \Phi(\mathcal{G}, \mathcal{Y}; \mathcal{C}^\alpha)$,

$$\tilde{\Phi}^{\text{def}} = \text{median}(\Phi^\alpha) \quad \text{and} \quad s^{\text{def}} = \text{median}(|\Phi^\alpha - \tilde{\Phi}|), \quad (\text{C9})$$

we mark a particle α as “failed” if

$$\Phi^\alpha > \tilde{\Phi} + 3s. \quad (\text{C10})$$

This excludes both non-finite and just “particularly anomalous” Φ^α .

Data Availability Statement

This work relied on the open-source software LESbrary.jl (Wagner et al., 2023) and Oceananigans.jl (Ramadhan et al., 2020; Wagner et al., 2025) to run the LES, Oceananigans.jl to run calibration simulations, and ParameterEstimote.jl (Wagner et al., 2022) and EnsembleKalmanProcesses.jl (Dunbar et al., 2022) for the Ensemble Kalman Inversion. Visualizations were made using Makie.jl (Danisch & Krumbiegel, 2021). Scripts for performing the calibration are available at the GitHub repository github.com/glwagner/Single-ColumnModelCalibration.jl (Wagner, 2024).

Acknowledgments

This project is supported by Schmidt Sciences, LLC and by the National Science Foundation grant AGS-1835576. N.C.C. is additionally supported by the Australian Research Council under DECRA Fellowship DE210100749 and the Center of Excellence for the Weather of the 21st Century CE230100012. Without implying their endorsement, we would also like to acknowledge useful conversations with Bruno Deremble, Alex Legay, Julien LeSommer, Qing Li, Brodie Pearson, Brandon Reichl, Roger Samelson, Luke Van Roekel, Dan Whitt, and Bill Young. Lastly, we like to acknowledge the three anonymous reviewers and Stephen Griffies for their constructive input that greatly improved the manuscript.

References

- Belcher, S. E., Grant, A. L., Hanley, K. E., Fox-Kemper, B., Van Roekel, L., Sullivan, P. P., et al. (2012). A global perspective on Langmuir turbulence in the ocean surface boundary layer. *Geophysical Research Letters*, 39(18), L18605. <https://doi.org/10.1029/2012GL052932>
- Blanke, B., & Delecluse, P. (1993). Variability of the tropical Atlantic Ocean simulated by a general circulation model with two different mixed-layer physics. *Journal of Physical Oceanography*, 23(7), 1363–1388. [https://doi.org/10.1175/1520-0485\(1993\)023<1363:VOTTAO>2.0.CO;2](https://doi.org/10.1175/1520-0485(1993)023<1363:VOTTAO>2.0.CO;2)
- Boccaletti, G., Ferrari, R., & Fox-Kemper, B. (2007). Mixed layer instabilities and restratification. *Journal of Physical Oceanography*, 37(9), 2228–2250. <https://doi.org/10.1175/jpo3101.1>
- Brenowitz, N. D., & Bretherton, C. S. (2019). Spatially extended tests of a neural network parametrization trained by coarse-graining. *Journal of Advances in Modeling Earth Systems*, 11(8), 2728–2744. <https://doi.org/10.1029/2019ms001711>
- Burchard, H. (2002). Energy-conserving discretisation of turbulent shear and buoyancy production. *Ocean Modelling*, 4(3–4), 347–361. [https://doi.org/10.1016/S1463-5003\(02\)00009-4](https://doi.org/10.1016/S1463-5003(02)00009-4)
- Burchard, H., & Bolding, K. (2001). Comparative analysis of four second-moment turbulence closure models for the oceanic mixed layer. *Journal of Physical Oceanography*, 31(8), 1943–1968. [https://doi.org/10.1175/1520-0485\(2001\)031<1943:CAOFSM>2.0.CO;2](https://doi.org/10.1175/1520-0485(2001)031<1943:CAOFSM>2.0.CO;2)
- Burchard, H., Bolding, K., Kühn, W., Meister, A., Neumann, T., & Umlauf, L. (2006). Description of a flexible and extendable physical–biogeochemical model system for the water column. *Journal of Marine Systems*, 61(3–4), 180–211. <https://doi.org/10.1016/j.jmarsys.2005.04.011>
- Canuto, V. M., Howard, A., Cheng, Y., & Dubovikov, M. (2001). Ocean turbulence. Part I: One-point closure model—Momentum and heat vertical diffusivities. *Journal of Physical Oceanography*, 31(6), 1413–1426. [https://doi.org/10.1175/1520-0485\(2001\)031<1413:otiop>2.0.co;2](https://doi.org/10.1175/1520-0485(2001)031<1413:otiop>2.0.co;2)
- Caulfield, C. (2021). Layering, instabilities, and mixing in turbulent stratified flows. *Annual Review of Fluid Mechanics*, 53(1), 113–145. <https://doi.org/10.1146/annurev-fluid-042320-100458>
- Caulfield, C.-c. P. (2020). Open questions in turbulent stratified mixing: Do we even know what we do not know? *Physical Review Fluids*, 5(11), 110518. <https://doi.org/10.1103/PhysRevFluids.5.110518>
- Cleary, E., Garbuno-Inigo, A., Lan, S., Schneider, T., & Stuart, A. M. (2021). Calibrate, emulate, sample. *Journal of Computational Physics*, 424, 109716. <https://doi.org/10.1016/j.jcp.2020.109716>
- Craik, A. D. D., & Leibovich, S. (1976). A rational model for Langmuir circulations. *Journal of Fluid Mechanics*, 73(3), 401–426. <https://doi.org/10.1017/S0022112076001420>
- Danisch, S., & Krumbiegel, J. (2021). Makie.jl: Flexible high-performance data visualization for Julia. *Journal of Open Source Software*, 6(65), 3349. <https://doi.org/10.21105/joss.03349>
- Deardorff, J. W. (1970). Convective velocity and temperature scales for the unstable planetary boundary layer and for Rayleigh convection. *Journal of the Atmospheric Sciences*, 27(8), 1211–1213. [https://doi.org/10.1175/1520-0469\(1970\)027<1211:CVATSF>2.0.CO;2](https://doi.org/10.1175/1520-0469(1970)027<1211:CVATSF>2.0.CO;2)
- Dunbar, O. R., Lopez-Gomez, I., Garbuno-Inigo, A., Huang, D. Z., Bach, E., & Wu, J. (2022). EnsembleKalmanProcesses.jl: Derivative-free ensemble-based model calibration. *Journal of Open Source Software*, 7(80), 4869. <https://doi.org/10.21105/joss.04869>
- Duraisamy, K. (2021). Perspectives on machine learning-augmented Reynolds-averaged and large eddy simulation models of turbulence. *Physical Review Fluids*, 6(5), 050504. <https://doi.org/10.1103/physrevfluids.6.050504>
- DuVivier, A. K., Large, W. G., & Small, R. J. (2018). Argo observations of the deep mixing band in the Southern Ocean: A salinity modeling challenge. *Journal of Geophysical Research: Oceans*, 123(10), 7599–7617. <https://doi.org/10.1029/2018jc014275>
- Frezat, H., Le Sommer, J., Fablet, R., Balarac, G., & Lguensat, R. (2022). A posteriori learning for quasi-geostrophic turbulence parametrization. *Journal of Advances in Modeling Earth Systems*, 14(11). <https://doi.org/10.1029/2022ms003124>

- Garanaik, A., Pereira, F. S., Smith, K., Robey, R., Li, Q., Pearson, B., & Van Roekel, L. (2024). A new hybrid mass-flux/high-order turbulence closure for ocean vertical mixing. *Journal of Advances in Modeling Earth Systems*, 16(1), e2023MS003846. <https://doi.org/10.1029/2023ms003846>
- Gardiner, C. W. (2021). *Elements of stochastic methods*. AIP Publishing.
- Gaspar, P., Grégoris, Y., & Lefevre, J.-M. (1990). A simple eddy kinetic energy model for simulations of the oceanic vertical mixing: Tests at station Papa and long-term upper ocean study site. *Journal of Geophysical Research*, 95(C9), 16179–16193. <https://doi.org/10.1029/jc095ic09p16179>
- Giordani, H., Bourdallé-Badie, R., & Madec, G. (2020). An eddy-diffusivity mass-flux parameterization for modeling oceanic convection. *Journal of Advances in Modeling Earth Systems*, 12(9), e2020MS002078. <https://doi.org/10.1029/2020ms002078>
- Gregg, M. C., D'Asaro, E. A., Riley, J. J., & Kunze, E. (2018). Mixing efficiency in the ocean. *Annual Review of Marine Science*, 10(1), 443–473. <https://doi.org/10.1146/annurev-marine-121916-063643>
- Gregory, J. M. (2000). Vertical heat transports in the ocean and their effect on time-dependent climate change. *Climate Dynamics*, 16(7), 501–515. <https://doi.org/10.1007/s003820000059>
- Griffies, S. M., Levy, M., Adcroft, A. J., Danabasoglu, G., Hallberg, R. W., Jacobsen, D., et al. (2015). Theory and numerics of the community ocean vertical mixing (cvmix) project. *Technical Reports Series*.
- Groeskamp, S., Griffies, S. M., Iudicone, D., Marsh, R., Nurser, A. G., & Zika, J. D. (2019). The water mass transformation framework for ocean physics and biogeochemistry. *Annual Review of Marine Science*, 11(1), 271–305. <https://doi.org/10.1146/annurev-marine-010318-095421>
- Gutjahr, O., Brüggemann, N., Haak, H., Jungclaus, J. H., Putrasahan, D. A., Lohmann, K., & von Storch, J.-S. (2021). Comparison of ocean vertical mixing schemes in the Max Planck Institute Earth System model (MPI-ESM1. 2). *Geoscientific Model Development*, 14(5), 2317–2349. <https://doi.org/10.5194/gmd-14-2317-2021>
- Häfner, D., Nuterman, R., & Jochum, M. (2021). Fast, cheap, and turbulent—Global ocean modeling with GPU acceleration in python. *Journal of Advances in Modeling Earth Systems*, 13(12), e2021MS002717. <https://doi.org/10.1029/2021ms002717>
- Harcourt, R. R. (2015). An improved second-moment closure model of Langmuir turbulence. *Journal of Physical Oceanography*, 45(1), 84–103. <https://doi.org/10.1175/jpo-d-14-0046.1>
- Held, I. M., Winton, M., Takahashi, K., Delworth, T., Zeng, F., & Vallis, G. K. (2010). Probing the fast and slow components of global warming by returning abruptly to preindustrial forcing. *Journal of Climate*, 23(9), 2418–2427. <https://doi.org/10.1175/2009jcli3466.1>
- Huang, N. E. (1979). On surface drift currents in the ocean. *Journal of Fluid Mechanics*, 91(1), 191–208. <https://doi.org/10.1017/s0022112079000112>
- Iglesias, M. A., Law, K. J., & Stuart, A. M. (2013). Ensemble Kalman methods for inverse problems. *Inverse Problems*, 29(4), 045001. <https://doi.org/10.1088/0266-5611/29/4/045001>
- Jungclaus, J. H., Lorenz, S. J., Schmidt, H., Brovkin, V., Brüggemann, N., Chegini, F., et al. (2022). The ICON earth system model version 1.0. *Journal of Advances in Modeling Earth Systems*, 14(4), e2021MS002813. <https://doi.org/10.1029/2021MS002813>
- Kantha, L. H., & Clayson, C. A. (1994). An improved mixed layer model for geophysical applications. *Journal of Geophysical Research*, 99(C12), 25235–25266. <https://doi.org/10.1029/94jc02257>
- Kovachki, N. B., & Stuart, A. M. (2019). Ensemble Kalman inversion: A derivative-free technique for machine learning tasks. *Inverse Problems*, 35(9), 095005. <https://doi.org/10.1088/1361-6420/ab1c3a>
- Kuhlbrodt, T., Jones, C. G., Sellar, A., Storkey, D., Blockley, E., Stringer, M., et al. (2018). The low-resolution version of HadGEM3 GC3.1: Development and evaluation for global climate. *Journal of Advances in Modeling Earth Systems*, 10(11), 2865–2888. <https://doi.org/10.1029/2018ms001370>
- Large, W. G., McWilliams, J. C., & Doney, S. C. (1994). Oceanic vertical mixing: A review and a model with a nonlocal boundary layer parameterization. *Reviews of Geophysics*, 32(4), 363–403. <https://doi.org/10.1029/94rg01872>
- Large, W. G., & Yeager, S. G. (2009). The global climatology of an interannually varying air–sea flux data set. *Climate Dynamics*, 33(2–3), 341–364. <https://doi.org/10.1007/s00382-008-0441-3>
- Legay, A., Deremble, B., & Burchard, H. (2024). Derivation and implementation of a non-gradient term to improve the oceanic convection representation within the k - ϵ parameterization.
- Lenain, L., & Pizzo, N. (2020). The contribution of high-frequency wind-generated surface waves to the Stokes drift. *Journal of Physical Oceanography*, 50(12), 3455–3465. <https://doi.org/10.1175/jpo-d-20-0116.1>
- Li, D. (2019). Turbulent Prandtl number in the atmospheric boundary layer—where are we now? *Atmospheric Research*, 216, 86–105. <https://doi.org/10.1016/j.atmosres.2018.09.015>
- Li, G., & Xie, S.-P. (2014). Tropical biases in CMIP5 multimodel ensemble: The excessive equatorial Pacific cold tongue and double ITCZ problems. *Journal of Climate*, 27(4), 1765–1780. <https://doi.org/10.1175/jcli-d-13-00337.1>
- Li, Q., Brüggemann, J., Burchard, H., Klingbeil, K., Umlauf, L., & Bolding, K. (2021). Integrating CVMix into GOTM (v6. 0): A consistent framework for testing, comparing, and applying ocean mixing schemes. *Geoscientific Model Development Discussions*, 2021(7), 1–30. <https://doi.org/10.5194/gmd-14-4261-2021>
- Li, Q., Reichl, B. G., Fox-Kemper, B., Adcroft, A. J., Belcher, S. E., Danabasoglu, G., et al. (2019). Comparing ocean surface boundary vertical mixing schemes including Langmuir turbulence. *Journal of Advances in Modeling Earth Systems*, 11(11), 3545–3592. <https://doi.org/10.1029/2019MS001810>
- Luyten, J., Pedlosky, J., & Stommel, H. (1983). The ventilated thermocline. *Journal of Physical Oceanography*, 13(2), 292–309. [https://doi.org/10.1175/1520-0485\(1983\)013<0292:vtv>2.0.co;2](https://doi.org/10.1175/1520-0485(1983)013<0292:vtv>2.0.co;2)
- Madec, G., Bourdallé-Badie, R., Bouttier, P.-A., Bricaud, C., Bruciaferri, D., Calvert, D., et al. (2017). NEMO ocean engine.
- McDougall, T. J., & Barker, P. M. (2011). Getting started with TEOS-10 and the Gibbs Seawater (GSW) oceanographic toolbox. *Scor/lapso WG*, 127, 1–28.
- McWilliams, J. C. (2016). Submesoscale currents in the ocean. *Proceedings of the Royal Society A: Mathematical, Physical and Engineering Sciences*, 472(2189), 20160117. <https://doi.org/10.1098/rspa.2016.0117>
- McWilliams, J. C., Huckle, E., & Shchepetkin, A. F. (2009). Buoyancy effects in a stratified Ekman layer. *Journal of Physical Oceanography*, 39(10), 2581–2599. <https://doi.org/10.1175/2009jpo4130.1>
- McWilliams, J. C., Sullivan, P. P., & Moeng, C.-H. (1997). Langmuir turbulence in the ocean. *Journal of Fluid Mechanics*, 334, 1–30. <https://doi.org/10.1017/s0022112096004375>
- Melet, A. V., Hallberg, R., & Marshall, D. P. (2022). Chapter 2 - The role of ocean mixing in the climate system. In M. Meredith & A. Naveira Garabato (Eds.), *Ocean mixing* (pp. 5–34). Elsevier. <https://doi.org/10.1016/B978-0-12-821512-8.00009-8>
- Mellor, G. L., & Yamada, T. (1982). Development of a turbulence closure model for geophysical fluid problems. *Reviews of Geophysics*, 20(4), 851–875. <https://doi.org/10.1029/rg020i004p00851>

- National Academies of Sciences, Engineering, and Medicine and others. (2022). Automated research workflows for accelerated discovery: Closing the knowledge discovery loop.
- Omand, M. M., D'Asaro, E. A., Lee, C. M., Perry, M. J., Briggs, N., Cetinić, I., & Mahadevan, A. (2015). Eddy-driven subduction exports particulate organic carbon from the spring bloom. *Science*, 348(6231), 222–225. <https://doi.org/10.1126/science.1260062>
- Prandtl, L., Wieselberger, C., & Betz, A. (1925). Results of the aerodynamic research institute in Göttingen (No. 1). *R. Oldenburg*.
- Pressel, K. G., Mishra, S., Schneider, T., Kaul, C. M., & Tan, Z. (2017). Numerics and subgrid-scale modeling in large eddy simulations of stratocumulus clouds. *Journal of Advances in Modeling Earth Systems*, 9(2), 1342–1365. <https://doi.org/10.1002/2016ms000778>
- Price, J. F., Weller, R. A., & Pinkel, R. (1986). Diurnal cycling: Observations and models of the upper ocean response to diurnal heating, cooling, and wind mixing. *Journal of Geophysical Research*, 91(C7), 8411–8427. <https://doi.org/10.1029/jc091ic07p08411>
- Ramadhan, A., Wagner, G. L., Hill, C., Campin, J.-M., Churavy, V., Besard, T., et al. (2020). Oceananigans.jl: Fast and friendly geophysical fluid dynamics on GPUs. *Journal of Open Source Software*, 4(44), 1965. <https://doi.org/10.21105/joss.01965>
- Rasp, S. (2020). Coupled online learning as a way to tackle instabilities and biases in neural network parameterizations: General algorithms and lorenz 96 case study (v1. 0). *Geoscientific Model Development*, 13(5), 2185–2196. <https://doi.org/10.5194/gmd-13-2185-2020>
- Rasp, S., Pritchard, M. S., & Gentile, P. (2018). Deep learning to represent subgrid processes in climate models. *Proceedings of the National Academy of Sciences*, 115(39), 9684–9689. <https://doi.org/10.1073/pnas.1810286115>
- Reffray, G., Bourdalle-Badie, R., & Calone, C. (2015). Modelling turbulent vertical mixing sensitivity using a 1-D version of NEMO. *Geoscientific Model Development*, 8(1), 69–86. <https://doi.org/10.5194/gmd-8-69-2015>
- Reichl, B. G., & Hallberg, R. (2018). A simplified energetics based planetary boundary layer (ePBL) approach for ocean climate simulations. *Ocean Modelling*, 132, 112–129. <https://doi.org/10.1016/j.ocemod.2018.10.004>
- Reichl, B. G., & Li, Q. (2019). A parameterization with a constrained potential energy conversion rate of vertical mixing due to Langmuir turbulence. *Journal of Physical Oceanography*, 49(11), 2935–2959. <https://doi.org/10.1175/jpo-d-18-0258.1>
- Reichl, B. G., Wittenberg, A. T., Griffies, S. M., & Adcroft, A. (2024). Improved equatorial upper ocean vertical mixing in the NOAA/GFDL OM4 model. *Authorea Preprints*.
- Saffman, P. G. (1970). A model for inhomogeneous turbulent flow. *Proceedings of the Royal Society of London. A. Mathematical and Physical Sciences*, 317(1530), 417–433.
- Sallée, J.-B., Shuckburgh, E., Bruneau, N., Meijers, A. J., Bracegirdle, T. J., & Wang, Z. (2013). Assessment of Southern Ocean mixed-layer depths in CMIP5 models: Historical bias and forcing response. *Journal of Geophysical Research: Oceans*, 118(4), 1845–1862. <https://doi.org/10.1002/jgrc.20157>
- Samelson, R. (2022). Wind drift in a homogeneous equilibrium sea. *Journal of Physical Oceanography*, 52(9), 1945–1967. <https://doi.org/10.1175/JPO-D-22-0017.1>
- Shu, C.-W. (2020). Essentially non-oscillatory and weighted essentially non-oscillatory schemes. *Acta Numerica*, 29, 701–762. <https://doi.org/10.1017/s0962492920000057>
- Siebesma, A. P., Soares, P. M., & Teixeira, J. (2007). A combined eddy-diffusivity mass-flux approach for the convective boundary layer. *Journal of the Atmospheric Sciences*, 64(4), 1230–1248. <https://doi.org/10.1175/JAS3888.1>
- Silvestri, S., Wagner, G. L., Campin, J.-M., Constantinou, N. C., Hill, C. N., Souza, A. N., & Ferrari, R. (2024). A new WENO-based momentum advection scheme for simulations of ocean mesoscale turbulence. *Journal of Advances in Modeling Earth Systems*, 16(7), e2023MS004130. <https://doi.org/10.1029/2023MS004130>
- Silvestri, S., Wagner, G. L., Constantinou, N. C., Hill, C. N., Campin, J.-M., Souza, A. N., et al. (2024). A GPU-based ocean dynamical core for routine mesoscale-resolving climate simulations. *Earth and Space Science Open Archive*. <https://doi.org/10.22541/essoar.171708158.82342448/v1>
- Smyth, W., & Moum, J. (2013). Marginal instability and deep cycle turbulence in the eastern equatorial Pacific Ocean. *Geophysical Research Letters*, 40(23), 6181–6185. <https://doi.org/10.1002/2013GL058403>
- Smyth, W., Pham, H., Moum, J., & Sarkar, S. (2017). Pulsating turbulence in a marginally unstable stratified shear flow. *Journal of Fluid Mechanics*, 822, 327–341. <https://doi.org/10.1017/jfm.2017.283>
- Souza, A. N., He, J., Bischoff, T., Waruszewski, M., Novak, L., Barra, V., et al. (2023). The flux-differencing discontinuous Galerkin method applied to an idealized fully compressible nonhydrostatic dry atmosphere. *Journal of Advances in Modeling Earth Systems*, 15(4), e2022MS003527. <https://doi.org/10.1029/2022MS003527>
- Souza, A. N., Wagner, G. L., Ramadhan, A., Allen, B., Churavy, V., Schloss, J., et al. (2020). Uncertainty quantification of ocean parameterizations: Application to the K-profile-parameterization for penetrative convection. *Journal of Advances in Modeling Earth Systems*, 12(12), e2020MS002108. <https://doi.org/10.1029/2020MS002108>
- Spalding, D. B. (1991). Kolmogorov's two-equation model of turbulence. *Proceedings of the Royal Society of London - Series A: Mathematical and Physical Sciences*, 434(1890), 211–216. <https://doi.org/10.1098/rspa.1991.0089>
- Suzuki, N., & Fox-Kemper, B. (2016). Understanding Stokes forces in the wave-averaged equations. *Journal of Geophysical Research: Oceans*, 121(5), 3579–3596. <https://doi.org/10.1002/2015JC011563>
- Taylor, G. I. (1922). Diffusion by continuous movements. *Proceedings of the London Mathematical Society*, 2(1), 196–212. <https://doi.org/10.1112/plms/s2-20.1.196>
- Taylor, J. R., & Thompson, A. F. (2023). Submesoscale dynamics in the upper ocean. *Annual Review of Fluid Mechanics*, 55(1), 103–127. <https://doi.org/10.1146/annurev-fluid-031422-095147>
- Thomas, L. N., Tandon, A., & Mahadevan, A. (2008). Submesoscale processes and dynamics. In *Ocean modeling in an eddy regime* (pp. 17–38). American Geophysical Union (AGU). <https://doi.org/10.1029/177GM04>
- Umlauf, L., & Burchard, H. (2003). A generic length-scale equation for geophysical turbulence models. *Journal of Marine Research*, 61(2), 235–265. Retrieved from https://elischolar.library.yale.edu/journal_of_marine_research/9
- Umlauf, L., & Burchard, H. (2005). Second-order turbulence closure models for geophysical boundary layers. A review of recent work. *Continental Shelf Research*, 25(7–8), 795–827. <https://doi.org/10.1016/j.csr.2004.08.004>
- Van Roekel, L., Adcroft, A. J., Danabasoglu, G., Griffies, S. M., Kauffman, B., Large, W. G., et al. (2018). The KPP boundary layer scheme for the ocean: Revisiting its formulation and benchmarking one-dimensional simulations relative to LES. *Journal of Advances in Modeling Earth Systems*, 10(11), 2647–2685. <https://doi.org/10.1029/2018MS001336>
- Venayagamoorthy, S. K., & Stretch, D. D. (2010). On the turbulent prandtl number in homogeneous stably stratified turbulence. *Journal of Fluid Mechanics*, 644, 359–369. <https://doi.org/10.1017/s002211200999293x>
- Von Kármán, T. (1931). *Mechanical similitude and turbulence* (No. 611). National Advisory Committee for Aeronautics.
- Wagner, G. L. (2024). glwagner/SingleColumnModelCalibration.jl. [Dataset]. *Zenodo*. <https://doi.org/10.5281/zenodo.14064823>

- Wagner, G. L., Hillier, A., & Constantinou, N. C. (2022). ParameterEstimocean.jl v0.14.2: Julia package for parameter estimation of turbulence closures for ocean models using Ensemble Kalman Inversion. <https://doi.org/10.5281/zenodo.5762810>
- Wagner, G. L., Ramadhan, A., Chor, T., Constantinou, N. C., Hillier, A., Lee, X. K., & Li, Q. (2023). LESbrary.jl: v0.1.1: Oceananigans large eddy simulation (LES) data for calibrating parameterizations [Dataset]. *LESbrary.jl: v0.1.1: Oceananigans large eddy simulation (LES) data for calibrating parameterizations*. <https://doi.org/10.5281/zenodo.7997002>
- Wagner, G. L., Silvestri, S., Constantinou, N. C., Ramadhan, A., Campin, J.-M., Hill, C., et al. (2025). *High-level, high-resolution ocean modeling at all scales with Oceananigans*. arXiv. <https://doi.org/10.48550/ARXIV.2502.14148>
- Whitt, D. B., Cherian, D. A., Holmes, R. M., Bachman, S. D., Lien, R.-C., Large, W. G., & Moum, J. N. (2022). Simulation and scaling of the turbulent vertical heat transport and deep-cycle turbulence across the equatorial Pacific cold tongue. *Journal of Physical Oceanography*, 52(5), 981–1014. <https://doi.org/10.1175/JPO-D-21-0153.1>
- Williams, R. G. (1991). The role of the mixed layer in setting the potential vorticity of the main thermocline. *Journal of Physical Oceanography*, 21(12), 1803–1814. [https://doi.org/10.1175/1520-0485\(1991\)021<1803:TROTML>2.0.CO;2](https://doi.org/10.1175/1520-0485(1991)021<1803:TROTML>2.0.CO;2)
- Wunsch, C., & Ferrari, R. (2004). Vertical mixing, energy, and the general circulation of the oceans. *Annual Review of Fluid Mechanics*, 36(1), 281–314. <https://doi.org/10.1146/annurev.fluid.36.050802.122121>
- Zhang, S., Fu, H., Wu, L., Li, Y., Wang, H., Zeng, Y., et al. (2020). Optimizing high-resolution community earth system model on a heterogeneous many-core supercomputing platform. *Geoscientific Model Development*, 13(10), 4809–4829. <https://doi.org/10.5194/gmd-13-4809-2020>